PAPER

Check for updates

Multivalent Cu catalytic sites on TiO₂ for efficient photocatalytic hydrogen evolution and mechanistic insights from solid-state *operando* photochemical analysis

Panagiotis Tzevelekidis, [ab] Elias Sakellis,[cd] Nikos Boukos,[c]
Alexandros K. Bikogiannakis,[e] Georgios Kyriakou, [e] Jakob Praxmair,[b]
Gregor A. Zickler,[b] Simone Pokrant [b] and Christiana A. Mitsopoulou [*a]

The global energy crisis has driven research into earth-abundant copper (Cu)-modified TiO₂ photocatalysts for the solar hydrogen evolution reaction (HER). Current high-performance TiO₂-based catalysts demonstrate optimal performance under UV light, which constitutes ∼5% of the solar spectrum. However, they exhibit negligible activity under illumination with longer wavelengths ($\lambda > 380$ nm), which represent ∼50% of solar spectra, hindering their practical application. Understanding dynamic catalyst/ co-catalyst interfacial changes and charge transfers is critical for optimization, yet progress is hindered by the need for expensive, specialized techniques lacking broad accessibility. We address these challenges by developing highly active photocatalysts featuring highly dispersed multivalent Cu active sites on surface-reduced TiO₂. Systematically controlling the amount of Cu loaded, we achieve one of the highest reported activities for transition metal-modified TiO₂, reaching 9.35 $mmol_{H_2} g_{cat}^{-1} h^{-1}$ under simulated solar light conditions and 1.23 $mmol_{H_2} g_{cat}^{-1}$ after 3 h under $\lambda > 380$ nm illumination. The AQY values were calculated to be 40.81% at 340 nm and 3.22% at 390 nm indicating the efficient utilization of simulated solar light especially in the UV-region. XPS, UV-DRS and HAADF-STEM confirm coexisting Cu^{1+}/Cu^{2+} species and ∼1.5 nm Cu_xO ($x = 1, 2$) nanoclusters, highly dispersed on the TiO₂ support. We further propose a solid-state *operando* UV-DRS approach enabling the direct observation of the dynamic, reversible reduction of Cu^x to Cu^0 under illumination, triggered by the charge transfer between TiO₂ and Cu^x. The photocatalyst displays remarkable stability, maintaining full activity for at least 26 hours of solar irradiation and retaining significant activity after 18 months in an aqueous/methanol dispersion. This work provides a design strategy for robust, high activity HER photocatalysts and an accessible *operando* platform for mechanistic studies in heterogeneous photocatalysis.

1. Introduction

The energy transition, which is not only associated with the issue of energy scarcity due to the depletion of fossil fuels, but also with the impact of their combustion on climate crisis, has been a topic of considerable discourse over the past decade. Concurrently, high-temperature chemical industrial processes,

aInorganic Chemistry Laboratory, Department of Chemistry, National and Kapodistrian University of Athens, 15771 Zografou, Greece. E-mail: cmitsop@chem. uoa.gr

bChemistry and Physics of Materials, University of Salzburg, Salzburg 5020, Austria

cInstitute of Nanoscience and Nanotechnology, National Centre of Scientific Research "Demokritos", Agia Paraskevi, 15341, Greece

dSection of Condensed Matter Physics, Department of Physics, National and Kapodistrian University of Athens, Athens, 15784, Greece

eDepartment of Chemical Engineering, University of Patras, Caratheodory 1, Patras, GR, 26504, Greece

which demand substantial energy inputs, have become increasingly costly, presenting significant challenges to sustainability. As a result, the scientific community has been extensively exploring alternative fuels to develop more sustainable and "green" processes.[1–5] Among the available energy sources, hydrogen (H₂) is regarded as one of the most promising due to its high energy density and potential to reduce harmful emissions during combustion, which are commonly associated with traditional fossil fuels.[6] Currently, H₂ is primarily produced through thermal catalytic reforming of fossil fuels and water electrolysis. However, a more sustainable approach is required for large-scale hydrogen production.[7] Solar light, a largely underutilized resource, presents an opportunity for efficient hydrogen production through photocatalysis, a process that converts solar energy into chemical energy.[8]

The utilization of photocatalytic processes can be traced back to the early 20th century; however, it was not until the

This journal is © The Royal Society of Chemistry 2025

J. Mater. Chem. A, 2025, **13**, 39859–39876 | **39859**

seminal work of Fujishima and Honda in the 1970s that the potential of semiconductor materials in heterogeneous catalysis for hydrogen generation was realized.[9] They demonstrated the photolysis of water under solar light using a single-crystalline titanium dioxide (TiO_2) electrode. Since then, numerous semi-conductors have been investigated for the hydrogen evolution reaction (HER), including metal oxides (*e.g.*, TiO_2 and ZnO), oxynitrides (*e.g.*, $TiON_x$), carbon-based catalysts (*e.g.*, g-C_3N_4), and perovskites.[10,11] Although direct water splitting through heterogeneous photocatalysis is a highly desirable approach for scalable hydrogen production, current catalysts suffer from low activity due to poor solar light utilization, fast exciton recom-bination, and limited reusability. TiO_2 remains a focal point in photocatalysis research due to its affordability, low toxicity, and high stability.[12-14] However, its wide bandgap (3–3.2 eV) constrains light absorption, reducing its overall efficiency.[15] Various strategies have been explored to overcome the limita-tions that hinder the applicability of TiO_2, including doping TiO_2 polymorphs with heteroatoms (*e.g.* Cu, Ag, Mn, and N) to narrow its bandgap, decorating TiO_2 with noble metal nano-particles (*e.g.* Pd, Ag, and Au) to exploit localized surface plas-mon resonance (LSPR) effects and forming heterojunctions with other semiconducting materials to leverage band align-ment for enhanced quantum efficiency and electron participa-tion in the reaction.[14,16-24]

Despite considerable progress in these strategies, no catalyst has yet been reported to achieve broad light absorption, high HER activity, and long-term stability simultaneously. This challenge is primarily attributed to fast exciton recombination and poor electron utilization. Given that photocatalysis is a surface-dependent process, an ideal photocatalyst should possess a high surface-to-volume ratio, precisely tailored cata-lytic centres, and efficient light absorption.[25]

The concept of highly dispersed metal catalysts, reaching even atomically dispersed sites *i.e.* single-atom catalysts, has gained considerable attention in catalysis and photocatalysis due to their ability to create uniform atomic-scale catalytic centres on semiconductor surfaces.[26] Transition metals, when reduced in size, exhibit unique catalytic properties, making them highly effective in photocatalytic or electrocatalytic processes such as CO_2 reduction, CO oxidation, H_2O_2 produc-tion, polyester plastics reforming, oxygen reduction reaction (ORR) and photocatalytic HER.[27-30] Platinum (Pt) has been widely regarded as the premier metal co-catalyst for the HER, owing to its optimal Fermi level position that facilitates the formation of a Schottky barrier with semiconductors like TiO_2 and CdS, thereby promoting efficient charge separation. Recent advancements highlight its continued efficacy; for instance, Cui *et al.*, reported a MoS_2–TiO_2 heterojunction where the loading of Pt nanoparticles enabled a dual-function system for simulta-neous benzaldehyde production and H_2 evolution (0.56 $mmol_{H_2}$ g_{cat}^{-1} h^{-1}) under simulated solar light.[31] In another study, a CdS/SiO_2 composite embedded within a ferroelectric PVDF, achieved remarkable H_2 evolution rates when loaded with Pt.[32] Despite this exceptional activity, the widespread, practical application of Pt remains constrained by its scarcity and high-cost, driving the search for earth-abundant alternatives.

Among transition metals, copper (Cu) is particularly attractive as a co-catalyst due to its cost-effectiveness compared to noble metals.[33-35] The development of highly dispersed Cu catalysts on TiO_2 has already shown promising results for the HER under solar light irradiation. For example, Zhang *et al.* synthesized Cu single-atom catalysts on TiO_2 with high apparent quantum efficiency (56% at 365 nm), utilizing MIL-125, a metal–organic framework (MOF) known for its high surface area and multiple Cu binding sites.[30] This resulted in a photocatalyst, with one of the highest reported HER activities under simulated solar light. An alternative approach involves using transition metals as dopants and as single-atom catalytic centres. This can be ach-ieved by doping of Cu^{2+} and the immobilization of atomic Cu centres or sub-nanometric nanoclusters, or through the inter-action of different energy bands, as seen with heteroatoms, such as N, along with the immobilization of Cu catalytic centres on TiO_2.[36-38] Both methods have been shown to result in significantly higher activity for the HER under simulated solar light. Another approach focuses on the role of different single-atom catalysts immobilized on TiO_2, such as Cu and Pr, in extending the lifetime of photogenerated electrons and facili-tating their transfer to Cu catalytic centres. In this way, the d- and f- orbitals of Cu and Pr, respectively, contribute to the electronic modification of the catalyst, leading to significantly higher activities for H_2 evolution compared to when each element is immobilized separately on TiO_2.[39]

Mechanistic insights into the reaction kinetics and the evaluation of structural and valence changes of Cu co-catalysts and TiO_2 support have predominantly relied on theoretical approaches. Density functional theory (DFT) calculations have been widely used to predict and rationalize the catalytic cycles for H_2 generation from a thermodynamic perspective. Numerous studies have explored the activation of TiO_2 under solar light, focusing on the mitigation of photogenerated elec-trons to reduce isolated Cu^{2+} ions to Cu^{1+}, followed by the reduction of adsorbed H_2O molecules to facilitate H_2 (g) generation.[40-43] In addition to theoretical calculations, EPR measurements have been employed to monitor the transition of Cu^{2+} ([Ar]$3d^9$) to the EPR-silent Cu^{1+} ([Ar]$3d^{10}$) upon light irra-diation.[30,44] Furthermore, *in situ* X-ray photoelectron spectros-copy (XPS) and X-ray absorption near edge structure (XANES) measurements have provided valuable insights into the changes in the oxidation state of Cu single-atom catalytic centers.[30,36,38,44,45] Despite significant advances in the field, challenges remain in experimentally studying the mechanisms of heterogeneous photocatalysis. The existing literature lacks experimental approaches that are not only cost-effective and easily accessible but also capable of elucidating the dynamic changes in Cu catalytic species on the TiO_2 surface under solar-light irradiation. Furthermore, such methodologies are essen-tial for investigating catalytic mechanisms in other heteroge-neous photocatalyst systems.

Herein, we report the synthesis of a robust photocatalyst for solar-driven HER composed of highly dispersed, multivalent Cu catalytic-sites supported on TiO_2. This catalyst exhibits excep-tional activity for H_2 evolution from water splitting under simulated solar light demonstrating high-activity even in the

39860 | *J. Mater. Chem. A*, 2025, **13**, 39859–39876

This journal is © The Royal Society of Chemistry 2025

near UV-visible range, with methanol employed as a hole scavenger (electron donor). Comprehensive structural and morphological characterization studies were conducted to elucidate the interaction between Cu species and the TiO_2 surface, as well as the impact of the synthetic procedure on TiO_2. A series of nanocomposites with varying Cu loadings were evaluated, and the most active photocatalyst was identified based on the HER performance. Long-term stability tests were conducted, along with an analysis of rate-limiting factors involving the catalyst and the sacrificial agent. Finally, we propose an all-solid-state *operando* approach for monitoring changes on the photocatalyst surface. This method enables real-time correlation of Cu valence state dynamics and electron donor interactions using UV-DRS measurements under simulated solar light irradiation.
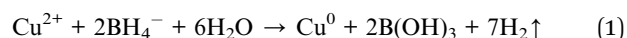
2. Results and discussion

2.1 Synthetic procedure rationale

The dispersed Cu active-sites on TiO_2 catalysts were synthesized using a facile sol–gel approach coupled with solvothermal treatment (Fig. 1). $TiO_x(OH)_{4-2x}$, the amorphous polymer formed by the spontaneous condensation of $Ti(OH)_4$ monomeric units, was chosen as the precursor to facilitate the direct deposition of Cu through the chemical reduction of the divalent copper precursor, $Cu(NO_3)_2 \cdot 3H_2O$. Since crystalline TiO_2 polymorphs exhibit high stability and resist the formation of surface defects under mild conditions or without the use of aggressive agents like HF, the amorphous precursor polymorph could potentially serve as a platform for the simultaneous generation of surface defects and the incorporation of reduced copper species. This is achieved through $NaBH_4$ induced reduction, enabling the development of highly dispersed metal active sites

on supports under controlled, non-corrosive conditions.[46,47] Additionally, calcination at high temperatures is known to reduce the pore size and limit the surface area due to the agglomeration of TiO_2 crystallites. In contrast, this synthetic procedure leverages the abundant binding sites available in the amorphous TiO_2 precursor, which are preserved under milder processing conditions, ensuring enhanced dispersion and immobilization of Cu-active sites. To further optimize the reaction environment, inert argon (Ar) gas was introduced into the dispersion in the Schlenk flask to effectively remove dissolved oxygen from the solution. This inert atmosphere prevents unwanted oxidation and prolongs the stability of surface defects, such as oxygen vacancies (O_{vac}) and Ti^{3+} sites, generated after the addition of the strong reductive agent, $NaBH_4$. These defects, in conjunction with crystal imperfections that result in kinks, steps, or terraces, play a critical role in stabilizing Cu at the required valence state for charge compensation. This is because Cu has been shown to have a high affinity for areas of support with higher electron density.[48]

The chemical reactions taking place after the introduction of $NaBH_4$ can be summarized using the following equations:

$$Cu^{2+} + 2BH_4^- + 6H_2O \rightarrow Cu^0 + 2B(OH)_3 + 7H_2\uparrow \quad (1)$$

$$Ti^{4+} + e^- \rightarrow Ti^{3+} \quad (2)$$

$$O^{2-} + 2e^- \rightarrow O_{vac} \quad (3)$$

2.2 Material characterization

2.2.1 Microstructure characterization and surface composition of the photocatalysts. Phase identification through PXRD
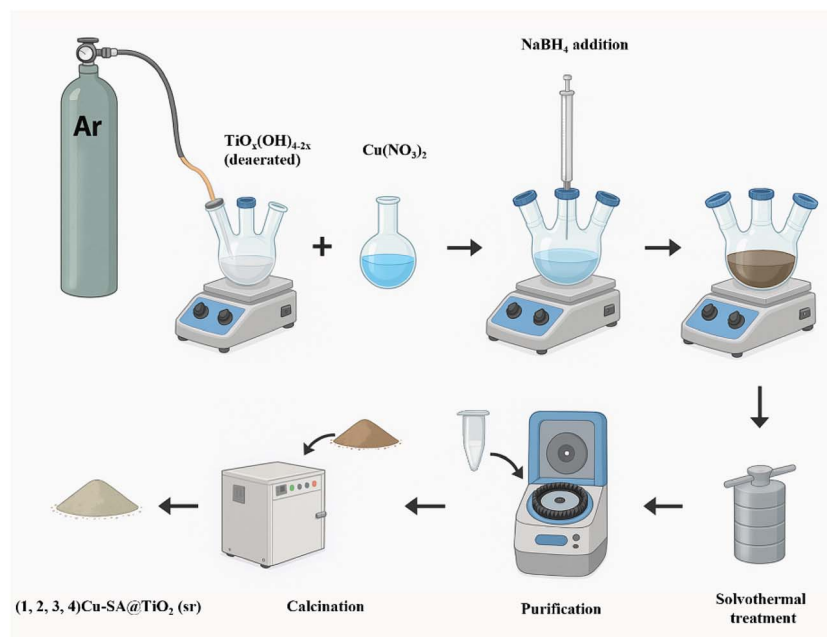

Fig. 1 Schematic representation of the synthetic procedure.

revealed that tetragonal anatase was the only detectable crystalline phase in all samples. Specifically, diffractions at 25.2°, 36.8°, 37.7°, 38.7°, 47.9°, 53.8°, 55°, 62.7°, 68.7°, 70.3°, 75.1°, 75.9° and 82.7° are assigned to the (101), (103), (004), (112), (200), (105), (211), (204), (116), (220), (215), (301) and (312) crystal planes of anatase (Fig. 2a). No diffraction peaks of zerovalent Cu or its oxides, CuO or Cu_2O, were observed even at the highest copper loading on the TiO_2 support. The absence of characteristic diffraction peaks for copper species in the XRD pattern suggests a high degree of Cu dispersion on the TiO_2 nanoparticle surface, likely in the form of isolated few-nanometric clusters. Alternatively, the copper clusters may be present at concentrations below the instrumental detection limit, further supporting the hypothesis of highly dispersed Cu species. To assess the potential incorporation of copper atoms and their surface doping in TiO_2, the position of the (101) plane was analyzed for each sample (Fig. 2b). The analysis revealed a negligible shift to lower 2θ angles, for the 1Cu-CS@TiO_2 (sr) sample relative to the unmodified TiO_2 (sr) reference. The absence of a significant shift suggests that no substantial lattice parameter change occurs, which would be expected if Cu^{2+} (0.087 nm) had substituted Ti^{4+} (0.074 nm) in the bulk crystal structure.[49] The observed minor shift is therefore attributed to an instrumental artifact, such as sample displacement during

analysis. This result further supports that copper species are not incorporated into the TiO_2 lattice but are instead dispersed on the catalyst surface and are available to participate in catalytic redox processes. Rietveld refinement of the diffraction patterns was employed to quantify any subtle changes in lattice parameters or strain resulting from ion substitution. Of note, the lattice parameters ($a = b, c$) of bare TiO_2 (sr) match the reported values of the ICSD card no. 142916 (Table S1). The observed microstrain value of 0.036% can be associated with the existence of oxygen vacancies (O_{vac}) located near Ti^{3+} ions, which predominantly reside within the bulk rather than on the surface of the nanoparticles. This is due to the inherent instability of undercoordinated Ti^{3+} ions at the elevated temperatures encountered during the calcination process in air, rendering their presence on the surface less favorable. The formation of a limited amount of such defects in the bulk structure contributes to the measured microstrain, reflecting localized lattice distortions caused by oxygen vacancies and Ti^{3+} interactions. These defects may originate from the strong reducing power of $NaBH_4$, which interacts with the polymeric amorphous precursor. This interaction may result in the cleavage of Ti–O bonds, creating lattice imperfections, which in turn could be incorporated into the nanoparticles during the assembly of larger TiO_2 nanoclusters, influencing their final structure and
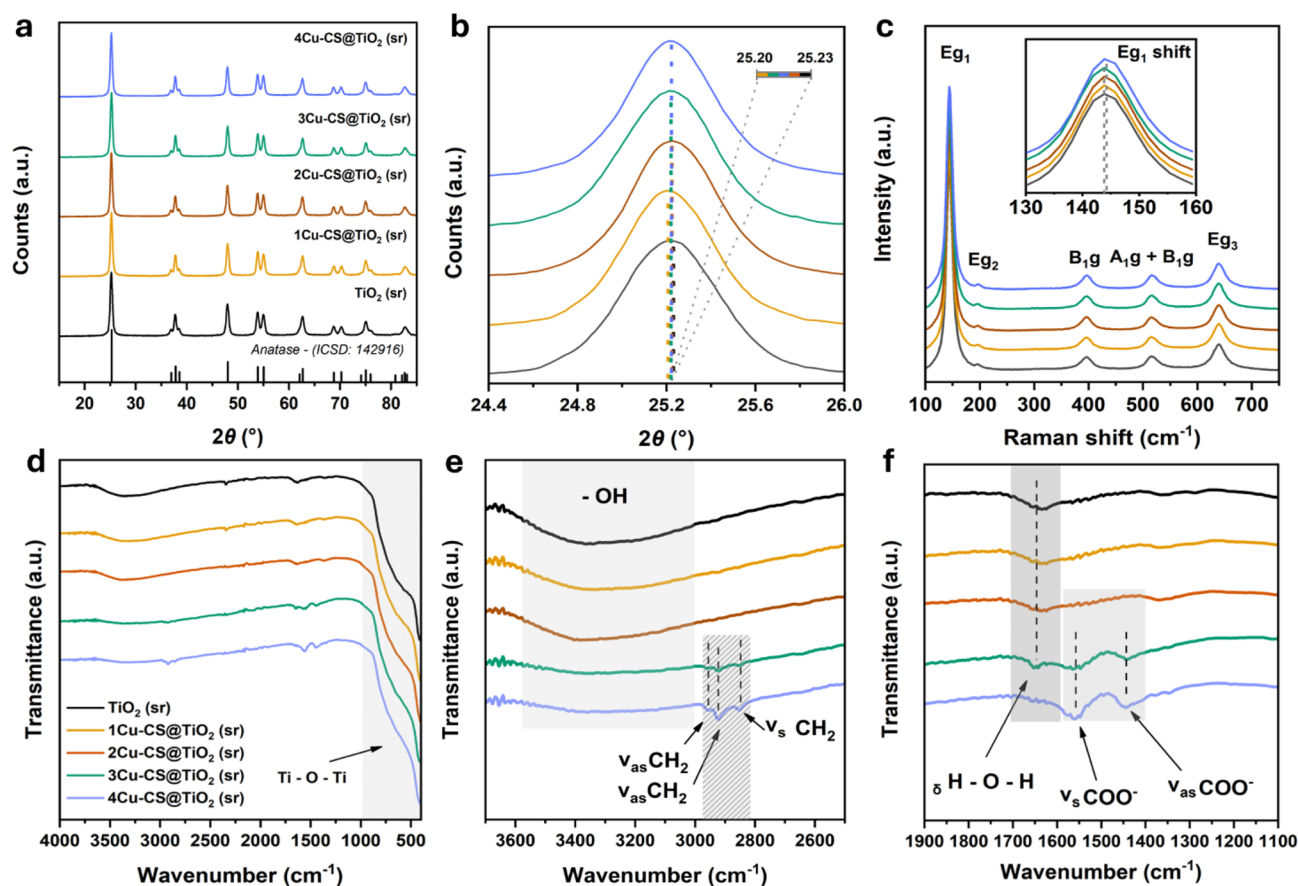

Fig. 2 (a) PXRD patterns of the synthesized photocatalysts. (b) Differences in the position of the diffraction attributed to the (101) plane of anatase as a result of Cu loading. (c) Raman spectra and shifting of the E_{1g} vibration of the crystal lattice of anatase. (d) Full IR-ATR spectra of the synthesized photocatalysts. (e) 1100–1900 cm^{-1} and (f) 2500–3700 cm^{-1} break-downs of the IR spectra.

39862 | J. Mater. Chem. A, 2025, **13**, 39859–39876

This journal is © The Royal Society of Chemistry 2025

properties and as a result increasing the microstrain value.[50,51] This observation is further supported by the trend in microstrain values, which correlates with the increasing $NaBH_4$ concentration and reaches a maximum for the 3Cu-CS@TiO$_2$ (sr) sample. The contribution of Cu to the lattice strain appears to be negligible in the case of bare TiO$_2$ (sr) and 3Cu-CS@TiO$_2$ (sr), as both samples were prepared using an equivalent amount of $NaBH_4$, resulting in comparable microstrain values. Additionally, increasing the $NaBH_4$ concentration in the presence of a higher Cu^{2+} precursor concentration (as in the 4Cu-CS@TiO$_2$ (sr) sample) did not significantly alter the microstrain value of the nanocomposite. This suggests that the copper species predominantly interacts with TiO$_2$ at the surface, with minimal bulk substitution of Ti^{4+} with Cu^{2+}. This surface-dominated interaction further indicates the limited incorporation of Cu into the bulk structure of TiO$_2$. Finally, the plateau in the microstrain value for the 3Cu-CS@TiO$_2$ (sr) sample indicates that further $NaBH_4$ addition does not introduce additional defects during the synthetic procedure, confirming no further impact on the Ti^{4+} and O^{2-} ions in the polymeric precursor. Unit cell volume calculations provide further insight into the location of the surface incorporated Cu atoms. Specifically, the anatase crystal lattice volume increases up to 2% mol Cu/Ti for 2Cu-CS@TiO$_2$ (sr), primarily due to the unit cell expansion along the a, b and especially the c-axis (Table S1).[52] This observation could further suggest a subtle anisotropic distortion of the anatase lattice along the c-axis, likely attributed to Cu atoms preferentially occupying positions along this direction. The crystallite size of the TiO$_2$ nanoparticles remained largely unaffected by the introduction of the copper precursor in the solution, further demonstrating that Cu primarily interacts with the surface of TiO$_2$. This results in a decoration-mediated modification rather than a doping effect, which could potentially alter the average crystallite size. In our case, the average crystallite size of the synthesized photocatalysts ranged from 17.4 ± 0.4 (for 1Cu-CS and 3Cu-CS@TiO$_2$ (sr)) to 18.8 ± 0.4 nm (for the sample 2Cu-CS@TiO$_2$ (sr)).

Raman spectroscopy was employed to further investigate possible changes in the vibrations of the anatase crystal lattice upon increasing the Cu concentration. The absence of vibrations of the crystalline phases of CuO or Cu$_2$O further supports the argument that copper exists in a highly dispersed state, as amorphous or sub-nanometric crystalline nanoclusters on the TiO$_2$ surface. Vibrations at 144, 196, 397, 517 and 639 are assigned to the three E_g modes and A_{1g} and B_{1g} modes of the anatase crystal lattice (Fig. 2c).[14] The inset in Fig. 2c indicates a negligible shift in the E_{1g} band of TiO$_2$, which is the most prominent in the 4Cu-CS@TiO$_2$ sample. This subtle shift suggests a slight shortening of Ti–O bond distances due to the minimal substitution of Ti^{4+} ions by Cu^{2+} or Cu^{1+} ions.[53] Even at low concentrations, Cu incorporation introduces localized strain, slightly compressing the Ti–O bonds and causing the observed shift. This effect aligns with the anisotropic behavior of the anatase lattice, where the c-axis is the most susceptible to structural modifications, while the a and b lattice constants remain largely unaffected. The stability of the a and b axes further supports the hypothesis that Cu incorporation is limited

and primarily affects the local bonding environment rather than inducing significant bulk lattice distortion.[54]

To analyze the chemical species present on the surface of the synthesized photocatalysts, we employed IR-ATR spectroscopy. The characteristic Ti–O stretching vibrations, originating from the TiO$_6$ octahedra within the anatase unit cell, were observed in the spectral region of 400–900 cm^{-1} for all samples, as illustrated in Fig. 2d. The bending vibration of the –OH groups bound to TiO$_2$ at 3300 cm^{-1} is evident in all samples, though its intensity decreases as the copper concentration increases. The most intense vibration is observed in the TiO$_2$ (sr) sample, indicating an abundance of binding sites such as terminal Ti atoms, Ti^{3+} ions, oxygen vacancies, or bridging oxygen atoms, which serve as favorable sites for hydroxyl group binding.[55] This outcome can be ascribed to the specific interaction of copper with the surface sites where –OH groups would typically bind, thereby reducing their availability for binding of the hydroxyl group. Consequently, as the copper content increases, the concentration of surface –OH groups decreases, reflecting the competitive binding between copper species and –OH groups on the TiO$_2$ surface (Fig. 2e). In addition to the hydroxyl groups, a weak vibration at 1637 cm^{-1} corresponds to the bending modes of O–H bonds in adsorbed water molecules, indicating the presence of water on the surface of the nanocatalysts (Fig. 2f).[56] Two distinct bands centered at 1440 cm^{-1} and 1556 cm^{-1} arise from the symmetric (ν_s) and asymmetric (ν_{as}) stretching vibrations of carboxylate (COO$^-$) ions, respectively (Fig. 2f). The absence of a band at 1700 cm^{-1}, which would correspond to the C=O stretching of free acetic acid, suggests that acetic acid is not adsorbed on the surface of the nanocatalysts.[57] Instead, the observed bands indicate the presence of coordinated acetate ions bound to surface atoms of the TiO$_2$ nanoparticles. The bands at 2849 cm^{-1} and 2924 cm^{-1} can be assigned to the symmetric and asymmetric C–H stretching vibrations of –CH$_2$ groups, while the band at 2957 cm^{-1} originates from the asymmetric C–H stretching vibrations of –CH$_3$ groups.[58] Notably, the intensity of these bands increases with increasing concentration of dispersed copper species, suggesting a strong correlation between the presence of copper and the adsorption of organic species, such as acetate ions and hydrocarbon fragments, on the surface of the nanocatalysts. One plausible explanation for this observation is that copper species, which through the synthetic procedure that was employed, can exist in three different valence states Cu^0, Cu^{1+} or Cu^{2+} and play a key role in the adsorption process. Specifically, Cu^{2+} ions exhibit a high affinity for complexation with carboxylate groups (e.g., acetate ions) due to their strong Lewis acidity and ability to form stable coordination complexes.[59] As the concentration of dispersed copper increases, the proportion of Cu^{2+} ions likely becomes more significant, particularly in the 3Cu-CS and 4Cu-CS@TiO$_2$ samples. This increase in Cu^{2+} concentration enhances the adsorption of acetate ions, leading to the observed increase in intensity of the carboxylate bands. While the presence of strong acetate-binding Cu^{2+} sites cannot be ruled out at lower copper concentrations, their number is likely lower compared to samples with higher copper loadings. This explains why the intensity of the carboxylate and C–H

This journal is © The Royal Society of Chemistry 2025

J. Mater. Chem. A, 2025, **13**, 39859–39876 | **39863**

stretching bands is more pronounced in samples with a higher copper content. The increase in intensity of these bands with increasing copper concentration indicates an increase in the availability of Cu^{2+} sites for complexation with acetate ions, stabilizing organic fragments on the surface of the nanocatalysts.

XPS analysis of the surface composition of the photocatalysts was used to reveal the valence state of Cu, providing insights into the chemical composition of the active surface in the resting state (rs) (*i.e.* before light illumination) (Fig. 3). High resolution scans in the B 1s region did not reveal the presence of adsorbed boron species, such as borates derived from the addition of $NaBH_4$, which could potentially inhibit catalytic activity. The consistent concentration of 0.7–0.9 wt% across the samples indicates that Na can be considered an invariant parameter and can therefore be ruled out as a contributor of potential different photocatalytic properties (Table S3). The C 1s region deconvolutes into four peaks at 284.8 eV (C–C, C–H) species, 286.0 eV (C–OH species), 287.6 eV (C=O formalities) and 288.8 eV (O–C=O species) (Fig. 3a).[60] The observed increase in the concentration of oxygenated carbon species with increasing copper concentration aligns well with the findings

from the IR-ATR spectra. This observation provides substantial evidence for the hypothesis that there is an increase in acetate groups, which are likely coordinated to Cu^{2+} or Cu^{1+} clusters on the surface of the TiO_2 support. In the Ti 2p region, as expected, titanium is present in the +4 oxidation state (TiO_2). The 2p doublet yields two peaks at 458.7 eV ($2p_{3/2}$) and 464.4 eV ($2p_{1/2}$), with a spin orbit splitting of 5.7 eV, all values characteristic for Ti^{4+}.[14,61] The Ti 2p and O 1s spectra do not show any clear signs of oxygen vacancies, which would appear as a shoulder at 457.3 eV for the Ti $2p_{3/2}$ line (Ti^{3+}).[61,62] However the presence of these vacancies in the bulk of the material cannot be excluded, as the vast majority of Ti will remain in the (Ti^{4+}) state, even after prolonged treatment (Fig. 3b). Regarding the O 1s XPS spectrum, it deconvolutes into two peaks: one at 530.0 eV, corresponding to the lattice oxygen of TiO_2, and another at 532.0 eV, attributed to surface hydroxyl species (–OH groups). As the copper concentration increases, the intensity of the hydroxyl peak decreases, following the trend observed in the IR-ATR spectra (Fig. 2e). This suggests that copper nanoclusters occupy the surface sites where –OH groups would preferentially adsorb. The copper $2p_{3/2}$ spectra are centered at 932.6 eV, which may be attributed to either oxidized (Cu^{1+}) copper or metallic
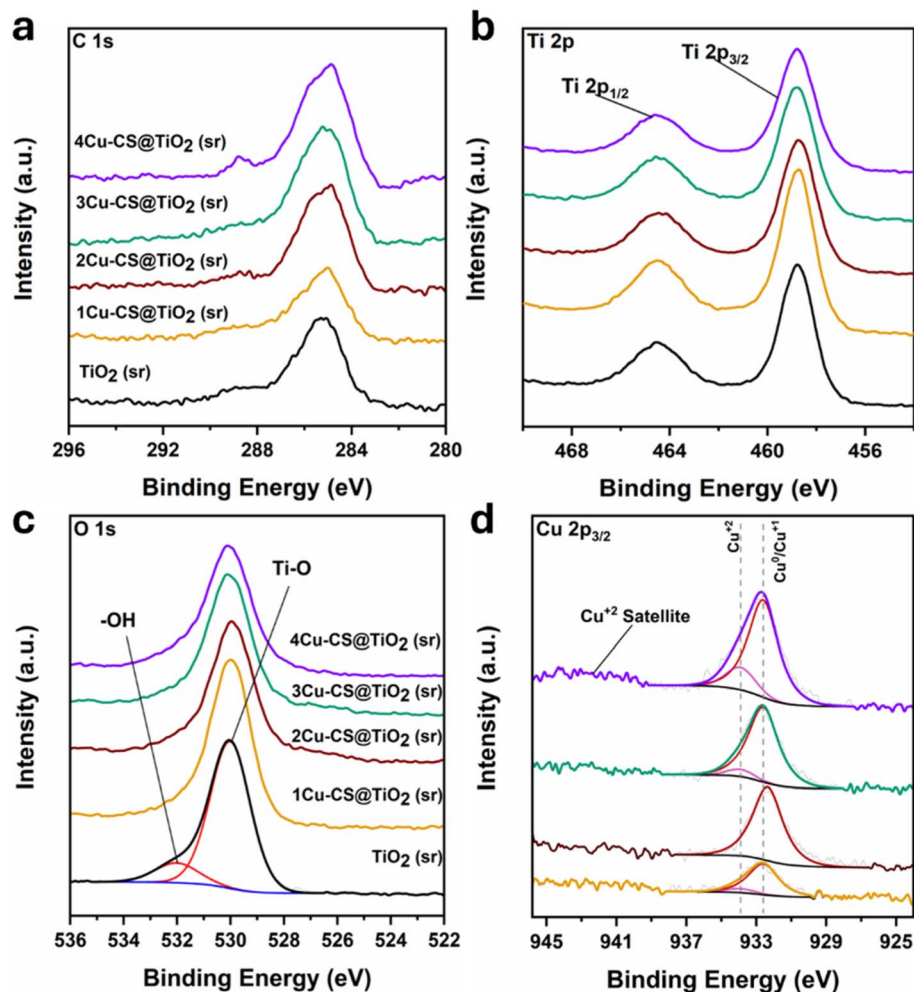

Fig. 3 XPS surface analysis of the synthesized photocatalysts. Selected regions for comparison of (a) C 1s (b) Ti 2p (c) O 1s and (d) Cu $2p_{3/2}$.

39864 | *J. Mater. Chem. A*, 2025, 13, 39859–39876

This journal is © The Royal Society of Chemistry 2025

(Cu^0) (Fig. 3d). Typically, to distinguish between these two states, the Cu 2p$_{3/2}$ binding energy is utilized in combination with the Cu LMM Auger kinetic energy in order to calculate the value of the modified Auger parameter (α').[63] However, in the present case, the low concentration of Cu in the samples leads to a very weak Cu LMM signal, which also overlaps with the Ti 2s region and cannot yield any meaningful information.[14,63] For 1Cu-CS@TiO$_2$ (sr), the binding energy of the main Cu 2p$_{3/2}$ line suggests that most likely the majority of Cu is either in the Cu^{1+} or metallic (Cu^0) state in the sample. In the case of 2Cu-CS@TiO$_2$ (sr), a mild shift to 932.3 eV is observed, which most likely suggests that Cu is mostly in the +1 oxidation state in this sample.[64] For samples 3Cu-CS@TiO$_2$ (sr) and 4Cu-CS@TiO$_2$ (sr), contributions also from Cu^{2+} are clearly evident due to the shoulder of the main Cu 2p$_{3/2}$ line at 933.9 eV. Specifically, for sample 4Cu-CS@TiO$_2$ (sr), Cu^{2+} contributions are estimated at *ca.* 10% of the total 2p$_{3/2}$ area. The fingerprint satellite peak for the Cu^{2+} state also appears at 942.6 eV, confirming the presence of such species in the samples, and most dominantly in sample 4Cu-CS@TiO$_2$ (sr).[61,65] This peak is not observed in any other sample during XPS analysis; however, the presence of minor concentrations of Cu^{2+} cannot be entirely ruled out, particularly for the 2Cu-CS@TiO$_2$ (sr) and 3Cu-CS@TiO$_2$ (sr) samples. These trace amounts of Cu^{2+} may be present but could fall below the instrument's detection limit, rendering them undetectable in the XPS spectra.

Transmission Electron Microscopy – Bright Field (TEM-BF) images were collected for all samples and analyzed to determine the size distribution of individual nanoparticles and the overall morphology (Fig. 4 and S2). The results indicate that all samples exhibit a polydisperse nature, with nanoparticle sizes ranging from 2 nm to 48 nm (Fig. S2b, S3b, S4b and S5b). This trend persists even in the TiO$_2$ (sr) sample, suggesting that the primary factor contributing to the polydispersity is the addition of NaBH$_4$.

The introduction of NaBH$_4$ alters the surface energy of TiO$_2$ nanoparticles, leading to uneven growth inhibition across the sample.[66] This non-uniform growth is further exacerbated by Ostwald ripening, where particles with higher surface defect concentrations (*e.g.*, Ti^{3+} sites) grow at the expense of smaller ones, resulting in larger nanoparticles exceeding 30 nm. Additionally, the presence of copper, whether as single atoms and/or nanoclusters, introduces a minor but statistically insignificant increase in the average crystallite size, as confirmed by both TEM and XRD analysis. This trend aligns with the XRD data, indicating that copper, in its single-atom or small-nanocluster form, has a limited impact on overall particle size distribution. The average nanoparticle size as calculated from the TEM images was 18.4 ± 9.5 nm for 3Cu-CS@TiO$_2$ (sr). High-angle annular dark-field scanning transmission electron microscopy (HAADF-STEM) combined with energy dispersive X-ray spectroscopy (STEM-EDS) was employed to investigate the distribution of copper (Cu) and identify the presence of aggregated species that could form clusters or nanoparticles (*e.g.*, Cu, Cu$_2$O, or CuO). The analysis of the Cu-EDS spectra and the overlaid EDS maps for Cu and Ti indicates that copper species are dispersed extensively on the surface of TiO$_2$ (sr) (Fig. 4c and

S3c, S4c, S5c). Despite increasing copper loading in the samples 3Cu-CS@TiO$_2$ (sr) and 4Cu-CS@TiO$_2$ (sr), the dispersion remains largely uniform, with only a few brighter spots observed, suggesting limited aggregation and the potential formation of copper nanoclusters. High-resolution transmission electron microscopy (HR-TEM) imaging was performed to investigate the presence of copper (Cu) and copper-based nanoparticles (*e.g.*, Cu, Cu$_2$O, or CuO) on the TiO$_2$ (sr) surface. For each sample, multiple *d*-spacings were calculated from HR-TEM images to identify crystallographic planes associated with TiO$_2$ and any potential copper-based phases. The analysis confirmed the presence of anatase TiO$_2$, with identified lattice planes corresponding to (101), (004) and (200) consistent with the tetragonal unit cell of anatase (Fig. 4d and S2d, S3d, S4d, S5d). In all samples, even those with higher copper loadings, no distinct *d*-spacings arising from unit cells of Cu^0 or copper-based (Cu$_2$O or CuO) crystalline nanoparticles were detected, indicating a high degree of dispersion of copper species on the TiO$_2$ (sr) surface.

The Cu loadings in the 1–4Cu-CS@TiO$_2$ (sr) catalysts were accurately quantified *via* ICP-OES, yielding the values of 0.98, 2.04, 2.34 and 2.96 wt% respectively (Table S2). These results confirm the successful incorporation of copper and are in good agreement with the semi-quantitative TEM-EDS analysis. Slight variations between the techniques are expected, as ICP-OES provides a precise bulk measurement, whereas EDS offers a localized, semi-quantitative composition. The consistency between the bulk-sensitive ICP-OES and the local EDS analysis confirms the uniform distribution of copper species throughout the bulk of each photocatalyst.[36]
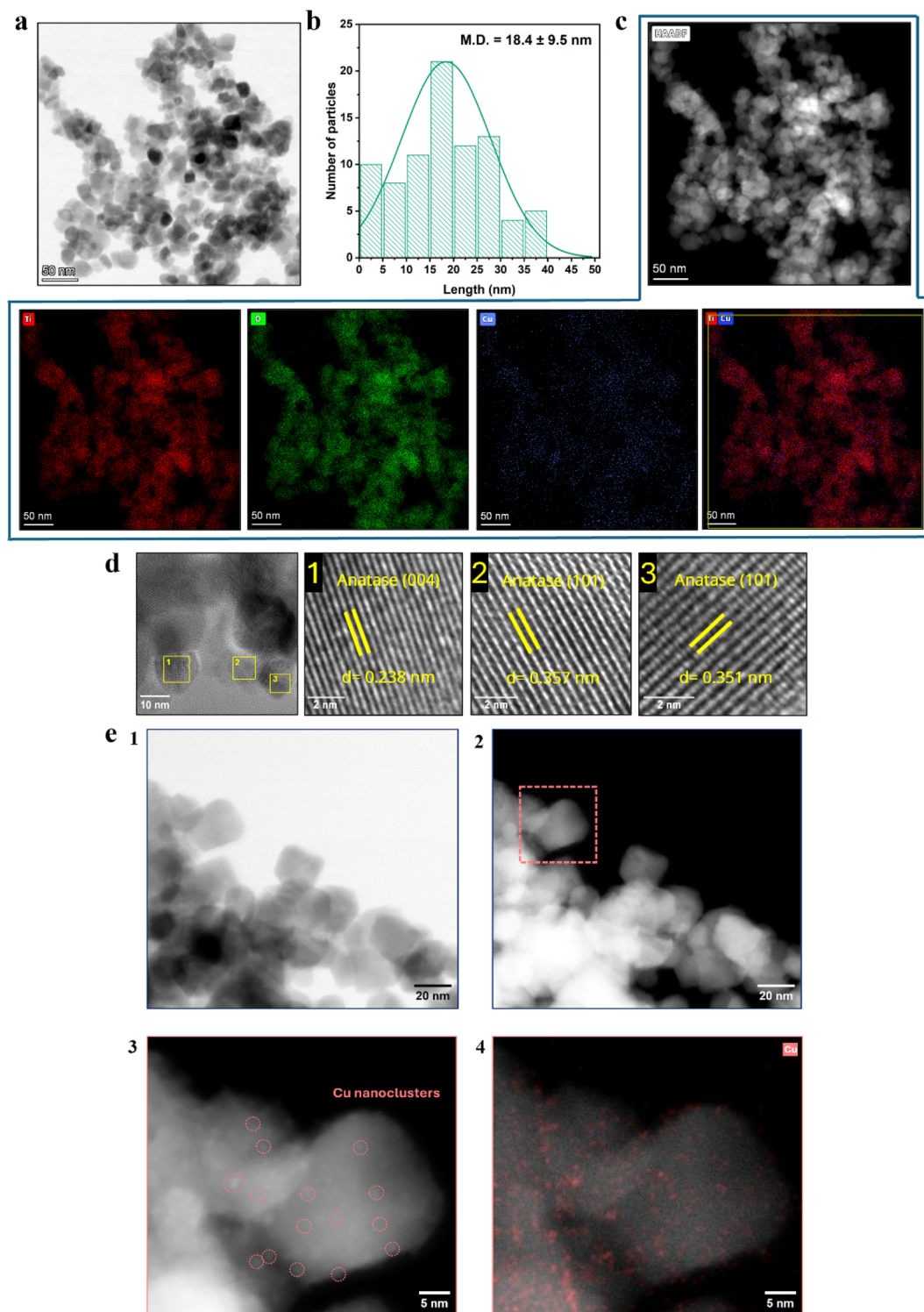
STEM-EDS mapping was utilized to quantitatively analyse the copper content on the TiO$_2$ (sr) surface (Table S2). The results show that the Cu concentration increases systematically with the addition of higher copper precursor amounts during synthesis, aligning well with the expected values. This outcome validates the effective copper loading on TiO$_2$ (sr), with measured concentrations reflecting controlled loading through the applied synthetic procedure. The presence of amorphous CuO or Cu$_2$O nanoclusters could not be definitively identified through HR-TEM, likely due to their extremely small size. However, their existence cannot be ruled out for the 3Cu-CS@TiO$_2$ (sr) and 4Cu-CS@TiO$_2$ (sr) samples, as evidenced by the more intense Cu signal in the STEM-HAADF spectrum (Fig. 4c and S5c).

To accurately determine the distribution of Cu on the TiO$_2$ surface, we used HAADF-STEM (Fig. 4e(1)–(3)) combined with STEM-EDS (Fig. 4e(4)). The HAADF-STEM images show bright contrast features corresponding to highly dispersed Cu nanoclusters with a uniform size distribution averaging 1.5 nm. The absence of larger nanoparticles suggests a strong stabilization of these nanoclusters on the TiO$_2$ surface, mediated by interactions with surface defects generated during the synthetic procedure, which prevented their aggregation.

2.2.2 Electronic properties. The optical properties of the synthesized photocatalysts were evaluated using UV-visible diffuse reflectance spectroscopy (UV-DRS). While many techniques commonly employed for characterizing surface-

This journal is © The Royal Society of Chemistry 2025

J. Mater. Chem. A, 2025, **13**, 39859–39876 | **39865**

Fig. 4 (a) TEM-BF image of catalyst 3Cu-CS@TiO$_2$ (sr). (b) Average size distribution of 80 particles measured through ImageJ software. (c) HAADF-STEM image and the corresponding STEM-EDS intensity elemental maps of the elements Ti, O and Cu in the STEM-BF image. (d) HR-TEM image and (1–3) lattice spacings of the selected regions. (e(1)) TEM-BF image, (2 and 3) HAADF-STEM images, and (4) Cu-STEM-EDS intensity elemental map overlay* with the STEM-HAADF image in (e(3)). *The above Cu signal intensity was obtained by applying three successive smoothing steps to the original STEM-EDS mapping data.

immobilized co-catalysts provide only partial information – often failing to distinguish the exact surface composition, particularly in the case of Cu, UV-DRS offers a complementary approach to elucidate the nature of surface-active sites and their interactions with the TiO$_2$ (sr) support. As shown in Fig. 5a and b, the synthesized photocatalysts exhibit additional optical

transitions beyond the intrinsic bandgap transition of TiO_2. These transitions are attributed to the presence of Cu species and defect states, which are consistent with the conditions of the synthetic procedure. Specifically, the strong reductive environment and the limited availability of dissolved oxygen (due to the Ar atmosphere) facilitated the formation of reduced Cu species (Cu^{1+} and Cu^0) while concurrently generating a limited number of defects, such as Ti^{3+} and oxygen vacancies, on the preexisting surface of the amorphous TiO_2 nanoparticles. These

defects were subsequently filled *in situ* by copper atoms, leading to the strong interaction between Cu and the TiO_2 support. Furthermore, the d–d transitions of Cu^{2+} are evident in all Cu-loaded samples, as observed in the DRS spectra, indicating the presence of multivalent copper across all compositions.[49] While XPS analysis revealed that Cu^{2+} is detectable at higher Cu loadings, this observation can be attributed to the instrumental limit of detection, particularly for samples with copper loadings below 3.09 wt% (refer to Table S2 for details). The absorption
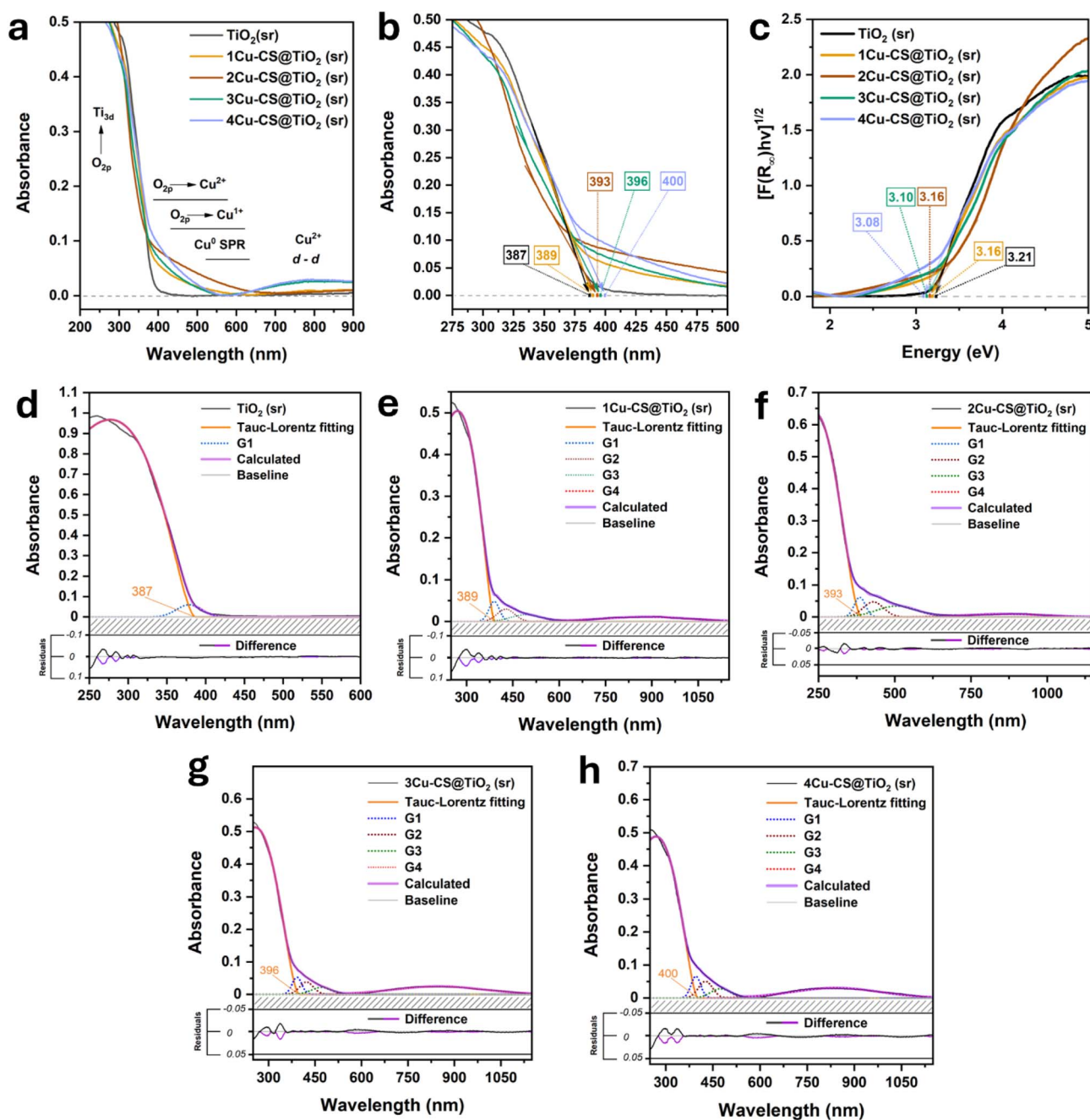

Fig. 5 (a) Absorption spectra of all the synthesized photocatalysts. (b) Differences in the absorption edge of TiO_2 upon Cu loading. (c) Kubelka–Munk plots for the determination of the bandgap of the synthesized photocatalysts. (d) Deconvoluted absorption spectra of TiO_2 (sr). (e) Deconvoluted absorption spectra of 1Cu-CS@TiO_2 (sr). (f) Deconvoluted absorption spectra of 2Cu-CS@TiO_2 (sr). (g) Deconvoluted absorption spectra of 3Cu-CS@$TiO2$ (sr). (h) Deconvoluted absorption spectra of 4Cu-CS@TiO_2 (sr).

This journal is © The Royal Society of Chemistry 2025

J. Mater. Chem. A, 2025, **13**, 39859–39876 | **39867**

edge of TiO_2 exhibits a minor shift to longer wavelengths, with the sample containing the highest Cu loading (4Cu-CS@TiO_2 (sr)) reaching 400 nm, compared to 387 nm for bare TiO_2 (sr). This minor shift suggests that there is no significant doping of Cu^{2+} or Cu^{1+} into the bulk lattice of TiO_2, which would otherwise introduce additional states deep within the bandgap of anatase TiO_2.[49] Instead, the observed effect is likely limited to the surface incorporation of Cu^{2+} or Cu^{1+} atoms at defect sites or interstitial positions, rather than extensive substitutional doping.[67] This surface incorporation may lead to localized electronic modifications but does not substantially alter the overall band structure of TiO_2. The Kubelka–Munk plots (Fig. 5c) derived from the transformed UV-DRS reflectance spectra (Fig. S6a) align with previous observations, showing that the bandgap of anatase TiO_2 undergoes only a minimal change upon Cu introduction. The bandgap follows a slight downward trend, reaching a minimum value of 3.08 eV for the sample with the highest Cu loading (4Cu-CS@TiO_2 (sr)). This finding further supports the conclusion that copper incorporation does not substantially modify the electronic structure of TiO_2 (sr). Rather, the minor bandgap reduction and the slight downward trend suggest that Cu species are predominantly located on the TiO_2 surface, where they remain accessible as active catalytic sites. This surface localization is consistent with the minor shifts observed in the absorption edge and the lack of substantial bandgap modification, reinforcing the idea that Cu incorporation is primarily a surface phenomenon rather than a bulk effect.[36]

For the investigation of the surface modifications of TiO_2 (sr) induced by Cu and the identification of the active copper species, deconvolution of the UV-DRS absorbance spectra was performed in conjunction with Kubelka–Munk plots, XRD, XPS, HR-TEM, and HAADF-STEM. Copper can exist in various oxidation states and coordination environments on TiO_2, including single-atom sites, metallic Cu nanoparticles, and oxide nanoclusters (e.g., Cu_2O and CuO). Using the bandgap value from Kubelka–Munk plots as a constraint, the Tauc–Lorentz function successfully deconvoluted the indirect bandgap transition (O 2p → Ti 3d).[68] Further analysis of the residual spectra using Gaussian functions provided insights into the copper species present, in line with the existing literature (Fig. 5d–h).[69–76] For bare TiO_2 (sr), an additional Gaussian peak (G1) centred at 378 nm (absorbance ~0.06), with a tail extending to 420 nm, was attributed to transitions from the valence band to defect states (e.g., O_{vac} or Ti^{3+}) near the conduction band (Fig. 5d and S6b).[77,78] This peak, associated with the Urbach effect, reflects disorder or defect states in the semiconductor, while its low intensity, compared to the main TiO_2 absorption (absorbance ~0.9), indicates limited defects, consistent with the minor modifications introduced by $NaBH_4$. In Cu-loaded samples, the highest defect concentration (indicated by the largest G1 peak height) was observed in 4Cu-CS@TiO_2, correlating with the highest $NaBH_4$/Ti ratio. This finding supports the conclusion that defects (e.g., O_{vac} or Ti^{3+}) arise from the reductive environment. A shift in the G1 peak position was also noted, with the 2Cu-CS@TiO_2 photocatalyst exhibiting a distinct defect formation process, as its peak did not shift to

longer wavelengths like the others (Fig. 5f and S6b). The G4 Gaussian fit, corresponding to the d–d transition of Cu^{2+} in an octahedral coordination environment, indicates the presence of surface-coordinated Cu^{2+} or CuO nanoclusters (Fig. 5d–h and S6e).[36,69–72,74,76,79,80] These species were identified in all samples, yet they became more pronounced at higher Cu loadings (3Cu-CS@TiO_2 and 4Cu-CS@TiO_2). For lower Cu loadings, the Cu^{2+} percentage fell below the XPS detection limit. The shifting of the G4 peak centre suggested the clustering of Cu^{2+} or agglomeration of CuO nanoparticles, which reduced the Jahn–Teller distortion with increasing Cu concentration.[69,70] The G2 peak, which corresponds to a combination of primarily Cu^{1+} and Cu^{2+} oxides, exhibits a relatively constant position but increases in width and intensity up to 1.93 wt% Cu (2Cu-CS@TiO_2) (Fig. 5d–h and S3c). At higher loadings (4Cu-CS@TiO_2 (sr)), the G2 peak becomes sharper and more intense. This observation indicates that isolated Cu^{1+} species, immobilized on TiO_2 (sr) surface defects or forming small Cu_2O clusters, are predominant at lower loadings. Conversely, with increasing Cu loading, the shift of G2 to shorter wavelengths and narrowing of the peak suggest agglomeration into larger Cu_2O and CuO nanoclusters. The G3 deconvoluted transition, centred from 492 to 506 nm, is attributed to metallic copper nanoparticles and their surface plasmon resonance (SPR) (Fig. 5d–h and S3d).[74,81] The increase in G3 width for 2Cu-CS@TiO_2 compared to 1Cu-CS@TiO_2 reflects the contribution of dispersed Cu^{1+} and Cu^0 SPR. The observed shift of G3 to longer wavelengths, such as 506 nm, is indicative of an increase in the size of the Cu nanoparticles. Furthermore, the shift of G3 to shorter wavelengths in the presence of higher Cu loadings suggests surface oxidation of the Cu nanoparticles to Cu_2O and CuO, thereby attenuating the SPR effect.

The charge transfer and separation efficiency of photogenerated charge carriers was further investigated through photoelectrochemical measurements. The transient photocurrent responses of bare TiO_2 (sr) and Cu-loaded catalysts are presented in Fig. S7a. All Cu-modified samples demonstrated an enhanced photocurrent density compared to TiO_2 (sr), indicating more efficient electron–hole separation. Notably, the 3Cu-CS@TiO_2 (sr) photocatalyst exhibited the most pronounced response to simulated solar-light, generating a photocurrent approximately 5.3 times higher than that of TiO_2 (sr). This suggests that the specific wt% loading of Cu in this sample optimally facilitates charge separation. This result was further confirmed using the EIS plots, where the 3Cu-CS@TiO_2 (sr) catalyst displayed a reduced resistance value compared to bare TiO_2 (sr), indicating a more efficient electron transfer at the interface between the electrode and the electrolyte (Fig. S7b).[29,38]

2.3 Photocatalytic hydrogen evolution and *operando* photocatalytic mechanism determination

The photocatalytic hydrogen evolution reaction (HER) *via* water splitting was systematically evaluated across all synthesized catalysts to determine the influence of Cu loading on activity. As shown in Fig. 6a and b, 3Cu-CS@TiO_2 (sr) exhibited optimal performance under full-spectrum solar simulation (300 W Xe

39868 | J. Mater. Chem. A, 2025, 13, 39859–39876

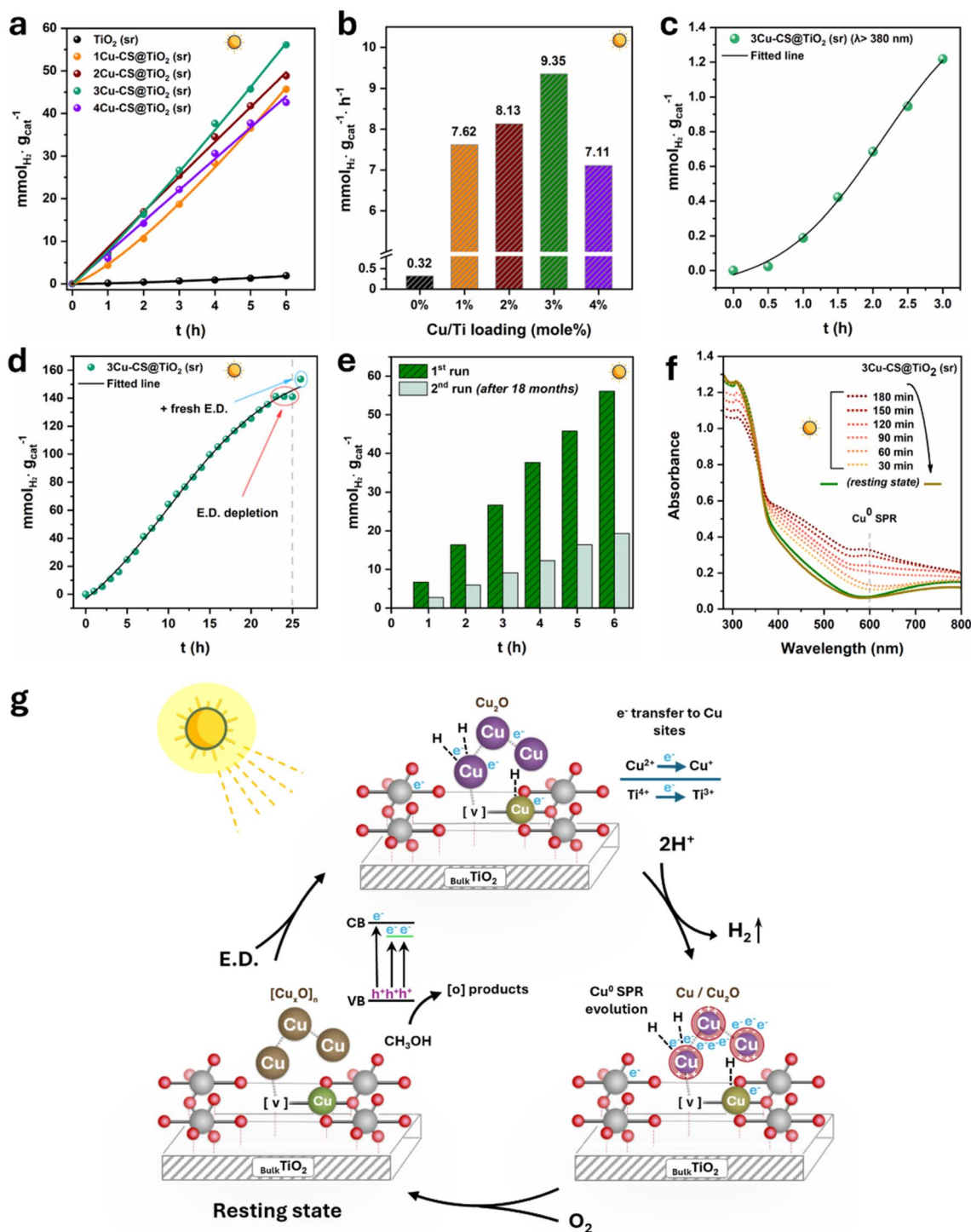This journal is © The Royal Society of Chemistry 2025

Fig. 6 (a) Performance of each synthesized photocatalyst for the photocatalytic HER under full solar light spectrum illumination over the course of 6 hours, (b) average H_2 evolution rate per hour for each photocatalyst, (c) photocatalytic HER with 3Cu-CS@TiO$_2$ (sr) under pure visible light (AM 1.5G filter + 380 nm cutoff), (d) photocatalytic HER with 3Cu-CS@TiO$_2$ (sr) over the course of 26 h solar light illumination for the determination of the rate limiting component, and (e) stability evaluation of the catalytic dispersion after 18 months. (f) Solid-state photochemical UV-DRS analysis of 3Cu-CS@TiO$_2$ (sr) and (g) schematic illustration of the transformations occurring on the photocatalytic surface of 3Cu-CS@TiO$_2$ (sr) during the solar-light driven HER.

lamp), achieving an average HER rate of 9.35 mmol$_{H_2}$ g$_{cat}^{-1}$, corresponding to a ~29-fold enhancement compared to bare TiO$_2$ (sr) (0.32 mmol$_{H_2}$ g$_{cat}^{-1}$ h^{-1}). This significant enhancement underscores the pivotal role of uniformly dispersed Cu

species in promoting charge separation and the H_2O reduction reaction. However, excessive Cu loading (4Cu-CS@TiO$_2$ (sr)) led to a decline in performance, likely due to nanocluster aggregation, which accelerates charge recombination and restricts

active-site accessibility, an outcome consistent with previously reported Cu-loaded photocatalysts.[75] Notably, under near UV-visible-light irradiation ($\lambda > 380$ nm), 3Cu-CS@TiO$_2$ (sr) retained important activity, generating 1.22 mmol$_{H_2}$ g$_{cat}^{-1}$ after 3 h (Fig. 6c). The herein reported activity of H$_2$ evolution with 3Cu-CS@TiO$_2$ (sr) ranks among the highest reported values for modified TiO$_2$ photocatalysts under both full solar light irradiation and after filtering most of the UV irradiation ($\lambda > 380$ nm) (Table S4).

The photon utilization efficiency of 3Cu-CS@TiO$_2$ (sr) was evaluated at the 340 and 390 nm centre wavelengths. A high AQY of 40.81% was achieved at 340 nm, indicating superior charge separation and transfer efficiency of the photocatalyst under high-energy UV irradiation.[30] The AQY value decreased substantially to 3.22% at 390 nm, a phenomenon directly correlated with the optical absorption of the photocatalyst, which exhibits an absorption edge at 396 nm (Fig. 5g). Nevertheless, this value remains high for a surface-modified TiO$_2$ system at this wavelength, indicating non-negligible activity under near-visible light.[35]

The catalyst with the highest H$_2$ catalytic activity, namely 3Cu-CS@TiO$_2$ (sir), was selected to determine surface changes during the photocatalytic reaction and its stability. Specifically, to examine the long-term stability and potential surface reorganization of active sites, we conducted extended photocatalytic testing under continuous solar irradiation. The photocatalyst exhibited remarkable durability, maintaining consistent activity over 26 hours. The temporal profile revealed a distinct plateau in hydrogen evolution after 23 hours of illumination, which we attribute to near-complete consumption of the methanol electron donor (E.D.) (Fig. 6d). This interpretation was verified by introducing 1 ml of deaerated 20% methanol solution, which promptly restored hydrogen production, as evidenced by the system reaching 153.7 mmol$_{H_2}$ g$_{cat}^{-1}$ by the 26 hour endpoint. To identify potential liquid-phase products from methanol oxidation that could inhibit catalytic activity, we performed GC analysis on aliquots taken at the start of the experiment (0 h), after 2 h and 12 h of irradiation, and at the 26th hour mark when H$_2$ evolution had ceased and before fresh MeOH had been added to the reaction solution (Fig. S8). The analysis identified formaldehyde (FAD) as the sole detectable oxidation product in the liquid phase. FAD was evident after 2 h of reaction, and its concentration increased substantially by the 12 hour timepoint. Interestingly, at the final measurement (26 h), the concentrations of both MeOH and FAD had significantly diminished. We attribute the simultaneous decrease to the high volatility of both compounds, particularly FAD (boiling point at −19 °C). Although FAD is known to potentially poison catalytic surfaces, its eventual depletion from the liquid phase suggests weak adsorption on 3Cu-CS@TiO$_2$ (sr) and indicates that catalyst poisoning from FAD is not the primary cause for the activity plateau at the 26th hour of simulated solar-light irradiation.[82,83] This controlled experiment in addition to the GC spectra of the liquid solution definitively demonstrates that the observed activity plateau resulted solely from electron donor depletion, confirming the exceptional structural and functional stability of the catalytic sites during prolonged operation. The absence of any irreversible deactivation indicates that the highly dispersed Cu active-sites and the Cu–TiO$_2$ interface remain intact and active throughout extended photocatalytic cycles. To assess long-term stability, the photocatalyst dispersion from the initial 6 hour experiment was stored in the dark for 18 months within the same reaction solution, without adding a fresh electron donor. When retested, the catalyst exhibited a ∼2.9-fold reduction in activity (Fig. 6e). This decline is attributed to the oxidation of Cu^{1+} species to less active Cu^{2+} by dissolved oxygen, surface contamination by organic byproducts such as formaldehyde from the initial methanol oxidation and the potential aggregation of copper nanoclusters into larger CuO nanoparticles that may act as charge recombination centers. Despite this loss of activity, the catalyst retained considerable functionality, maintaining a hydrogen evolution rate of 3.2 mmol$_{H_2}$ g$_{cat}^{-1}$ h^{-1}. This demonstrates that the material possesses promising long-term stability, remaining viable for photocatalytic applications even after extended storage in the reaction environment.

To gain further insights into the transformations occurring on the surface of 3Cu-CS@TiO$_2$ (sr), UV-DRS was employed. This method is sensitive to the coordination environment of metal ions (e.g., Cu^{2+}/Cu^{1+}/Cu^0) during the catalytic cycle for H$_2$ evolution, while keeping the catalyst in the solid state, allowing easy recovery for post-reaction analysis. Furthermore, the solid-state nature of the catalyst makes it easily retrievable for further evaluation. Using volatile methanol as the electron donor in our set-up enables a solid–gas interface and allows us to exploit the reduced reaction rate compared to dispersed nanocatalysts with readily accessible electron donors. This setup also provides a convenient way to observe surface-related phenomena. In our case, the catalytic surface undergoes important changes, as shown in Fig. 6f. Upon solar light activation, photogenerated holes (h$^+$) in the valence band (VB) of TiO$_2$ oxidize methanol gas adsorbed on the catalyst surface. Simultaneously, photogenerated electrons (e$^-$) from the conduction band (CB) of TiO$_2$ migrate to highly dispersed CuO/Cu$_2$O nanoclusters, reducing them to Cu^{1+} species and metallic Cu^0 nanoparticles.[84] This dual process drives the hydrogen evolution reaction while sustaining the catalytic cycle. Over time, a weak absorption band emerges at 600 nm, characteristic of the surface plasmon resonance (SPR) effect of metallic Cu^0 nanoparticles. This spectral feature develops alongside two additional contributions to the absorption profile (400–550 nm): interactions between Cu species and surface defects (particularly Ti^{3+} and oxygen vacancies (O$_v$) generated during TiO$_2$ photoactivation), and intraband transitions within the Cu^0 nanoparticles. The observed changes indicate that Cu^{2+} initially present as highly dispersed CuO nanoclusters strongly bound to the TiO$_2$ surface undergoes reduction to Cu^{1+} and eventually to Cu^0 nanoparticles. These nanoparticles further enhance the absorption properties of the photocatalyst, extending its light absorption range and enabling visible light harvesting through the SPR effect. After turning off the lamp and storing the photocatalyst in air overnight, we obtained a new absorption spectrum (brown-colored spectrum in Fig. 6f) representing the post-irradiation resting state of the photocatalyst. A comparison

39870 | J. Mater. Chem. A, 2025, 13, 39859–39876

This journal is © The Royal Society of Chemistry 2025

with the pre-irradiation spectra (green line) reveals nearly identical features, with only minor differences. Most notably, a slight decrease in intensity of the d–d transition band above 600 nm is observed, which is attributed to the partial, irreversible reduction of Cu^{2+} to Cu^+ during the photocatalytic reaction. This minimal spectral change suggests that the system exhibits remarkable stability under reaction conditions, with only limited permanent modification of the copper oxidation state.

Following the 6 hour hydrogen evolution experiment, the photocatalyst powder was recovered, washed with ethanol, and dried. For comparison purposes, we also analysed the post-reaction powder from the solid-state DRS photochemical study, which was examined without any cleaning treatment. All XRD patterns exclusively exhibited diffraction peaks corresponding to anatase TiO_2, with no detectable signals from metallic Cu^0 nanoparticles (Fig. S9). Both samples showed background curvature at 62.5° 2θ, which was significantly more pronounced in the H_2O/MeOH-dispersed sample. This feature likely originates from adsorbed MeOH and/or FAD, which contribute to the amorphous part of the diffraction pattern. Notably, the photocatalyst analysed *via* UV-DRS on its all-solid form demonstrated substantially less interference from organic species, highlighting the advantage of this approach for studying the intrinsic surface properties of TiO_2-based photocatalysts.

The combination of data obtained from the characterization of 3Cu-CS@TiO_2 (sr) and solid-state *operando* photochemical analysis leads us to propose the mechanism underlying the solar-light-driven HER in the presence of methanol (MeOH) as an electron donor (E.D.) (Fig. 6g).

In its resting state, the catalyst consists of strongly immobilized Cu_xO ($x = 1, 2$) nanoclusters on the TiO_2 surface. Upon exposure to solar light with a wavelength less than 393 nm, as illustrated in Fig. 5b, c and g, TiO_2 (sr) is activated, facilitating electron transfer into the conduction band (CB). The photogenerated charge carriers (h^+ and e^-) diffuse across the photocatalyst surface, where h^+ are scavenged by MeOH generating oxidation products and suppressing recombination with e^-. It is important to note that in this process, MeOH not only acts as an h^+ scavenger but also serves as a proton (H^+) source *via* its photocatalytic reforming to formaldehyde (FAD), contributing to the enhanced rate of H_2 evolution when coupled with H_2O reduction.[85,86] Subsequently, the e^- are transferred to the highly dispersed Cu catalytic sites, reducing Cu^{2+} to Cu^{1+} and facilitating strong H^+ adsorption on the Cu^{1+} active sites. The hydrogen evolution process is likely to occur *via* adsorbed hydrogen recombination (Langmuir–Hinshelwood) or a proton-coupled electron-transfer step (Heyrovsky), with the high dispersion of Cu sites favouring the former. *Operando* photocatalytic analysis reveals that, over time, surface plasmon resonance (SPR) emerges from metallic Cu^0 nanoparticles, which could be attributed to the aggregation of dispersed Cu sites into larger Cu^0 nanoparticles. However, the absorption spectra of the used photocatalyst's resting state show minimal differences from the fresh catalyst, suggesting that SPR originates from the outer-shell reduction of Cu_xO nanoclusters to

metallic Cu^0 rather than their aggregation. The combined effect of SPR from Cu^0 on the outer shell of Cu_xO nanoclusters enhances photocatalytic performance by broadening light absorption, accelerating electron diffusion and proton reduction to H_2.

3. Experimental section

3.1 Materials

Titanium(IV) i-propoxide – $Ti\{OCH(CH_3)_2\}_4$ – TTIP (97%), absolute ethanol – CH_3CH_2OH (99.8%), methanol – CH_3OH (99%), copper(II) nitrate trihydrate – $Cu(NO_3)_2\cdot3H_2O$ (99%), anhydrous acetic acid – CH_3COOH (99.8%), sodium borohydride – $NaBH_4$ (99.99%), and acetonitrile – (MeCN) (99.9%) – were purchased from Acros Organics and used without further purification. Barium sulfate – $BaSO_4$ (99%), was obtained from Thermo Fisher Scientific. 70% HNO_3, 34.5–36.5% H_2O_2 solution and 48% HF solution were obtained from Merck. 35% formaldehyde – CH_2O solution was obtained from Honeywell. Ultra-pure water was obtained from a Rephile Milli-Q water system and used for all the synthetic procedures. Argon – Ar gas (99.7%) was supplied by Revival N.C.

3.2 Synthesis of multi-valent Cu–TiO_2 (xCu-CS–TiO_2 (sr)) catalysts

A sol–gel synthetic procedure coupled with solvothermal treatment was employed for the synthesis of the Cu-CS@TiO_2 catalysts. For the synthesis of the amorphous $TiO_x(OH)_{4-2x}$ colloid dispersion, a synthetic procedure previously developed in our lab was employed.[14] Briefly, 1.5 ml (5 mmol) of TTIP were dropwise added to 10 ml of absolute ethanol in a round bottom flask, under continuous stirring. Stirring of the precursor solution for 30 min was followed by the addition of 0.6 ml (10 mmol) anhydrous acetic acid for controlling the hydrolysis rate of the titanium alkoxide solution. After the complete hydrolysis of the titanium precursor, 1 ml of Milli-Q H_2O was added with a rate of 0.5 ml min^{-1}. The previously transparent solution gradually turned cloudy yielding the $TiO_x(OH)_{4-2x}$ polymeric dispersion. As soon as the solution turned completely turbid, another 0.6 ml of anhydrous acetic acid and 4 ml of EtOH were added to avoid gelation of the dispersion. The reaction flask was kept for 8 h in the dark while maintaining constant stirring allowing the uniform nucleation and growth of amorphous particles.

xCu-CS–TiO_2 with different molar percentages ($x = 1, 2, 3$ or 4% mole Cu per mole Ti) were synthesized for identifying the most active catalyst for the HER, while surface reduced TiO_2 was synthesized without the addition of Cu precursor salt, for comparison. Necessary amounts of $Cu(NO_3)_2\cdot3H_2O$ for the theoretical molar of Cu were added to the dispersion and the solution was homogenized under constant stirring for 1 h. Next, the reaction flask was cooled to 4 °C using an ice bath inside a fume hood while Ar gas was continuously supplied through the dispersion. For the *in situ* reduction of Cu^{2+}, four molar equivalents of $NaBH_4$ were dissolved in 1 ml Milli-Q H_2O and rapidly injected into the $[Cu^{2+}]_x[TiO_x(OH)_{4-2x}]_y$ dispersion. The

This journal is © The Royal Society of Chemistry 2025

J. Mater. Chem. A, 2025, **13**, 39859–39876 | **39871**

dispersion instantly turned dark brown in color, and the reaction flask was kept for an additional 2 h at 4 °C while constant stirring was maintained to ensure complete reduction of Cu^{2+} and facilitate uniform interaction with $TiO_x(OH)_{4-2x}$. Following this, the reaction solution was transferred to a 30 ml Teflon lined autoclave reactor and subjected to solvothermal treatment for 8 h at 120 °C. The resulting pellet was thoroughly washed with ethanol and water using multiple centrifugation and redispersion cycles, until the pH of the supernatant reached 6.8. Finally, the products were calcined at 550 °C for 2 h to induce crystallization of the catalysts and eliminate residual carbon impurities. The synthesized samples of the Cu co-catalysts immobilized on the surface of reduced (sr) TiO_2 were denoted as 1, 2, 3, 4Cu-CS@TiO_2 (sr).

3.3 Characterization methods

Powder X-ray diffraction (PXRD) patterns of the synthesized catalysts were recorded on a Bruker D8 Advance diffractometer, using Bragg–Brentano geometry, operating at 40 kV and 25 mA. A Cu anode with $K\alpha_1$ ($\lambda = 1.5418$ Å) was used as the X-ray source of the instrument. The diffraction patterns were recorded in the 3–85° 2θ range while the step size was set at $0.02°$ s^{-1} and the step duration at 0.220 s. Crystalline phase identification was performed using Diffrac.EVA software while Rietveld refinement was carried out using Diffrac.TOPAS. Crystallite size was determined by fitting the most prominent diffraction peak of anatase located at 25.3° (101) and employing the Scherrer equation:

$$L = \frac{K\lambda}{B(2\theta)\cos\theta}, \tag{4}$$

where K represents the shape factor (0.89 for spherical nanocrystallites), λ denotes the wavelength of the X-rays originating from the Cu anode, $B(2\theta)$ corresponds to the full-width at half-maximum (FWHM) of the diffraction assigned to the (101) crystal plane of anatase and θ represents the Bragg angle.

Raman spectroscopy of the nanocatalysts was carried out with a dual-source Micro-Raman Renishaw inVia Qontor spectrometer using a 532 nm Ar laser.

Fourier Transform Infrared (FT-IR) spectroscopy was performed using a Shimadzu IRAffinity-1 spectrometer equipped with an ATR (attenuated total reflection) accessory. The technique was utilized to characterize the powdered catalysts and for the evaluation of the photochemical events on the surface of the catalyst.

XPS measurements were performed in an ultra-high vacuum (UHV) chamber with a working pressure of 5×10^{-10} mbar. A non-monochromatic Al Kα radiation source (1486.6 eV) and a Leybold LH EA11 electron energy analyzer, operated at a pass energy of 100 eV, were used. Catalyst powders were pressed on a thin lead sheet to prepare the samples. The analysis area was a rectangular region measuring 4×5 mm^2, and binding energies were determined with an accuracy of 0.1 eV. All spectra were charge-corrected using the adventitious carbon peak (C 1s) at 284.8 eV as a reference.

UV-DRS absorbance and reflection spectra were recorded on a SHIMADZU UV-2600i spectrophotometer equipped with an integrating sphere attachment (ISR-2600Plus) using $BaSO_4$ as a reference. For the measurements, 1:10 mixtures of the powdered catalyst and $BaSO_4$ were prepared and used for the determination of the absorption and reflection maximum of the powdered samples. The reflection data were transformed to Kubelka–Munk plots for the estimation of the bandgap of the semiconductor nanocatalysts. The plots were created by plotting $(F(R_\infty)h\nu)^{1/2}$ versus the photon energy and extrapolating the linear fit of the steep part of the plot below 390 nm to the point of zero photon energy.

The Tauc–Lorentz model (5) was used to fit the indirect bandgap transition of anatase TiO_2 in the UV-DRS spectra.[87] This model combines the Tauc law, which describes the absorption edge of semiconductors, with the Lorentz oscillator model, which accounts for the broadening of electronic transitions due to interactions with the lattice. For each sample, the Tauc–Lorentz function was applied to accurately model the fundamental absorption edge of TiO_2, ensuring that the indirect bandgap transition (O 2p → Ti 3d) was properly represented. The fitting process involved constraining the bandgap energy to the value obtained from the Kubelka–Munk plots, allowing for a precise deconvolution of the TiO_2 absorption edge while isolating contributions from defect states (Ti^{3+} or O_{vac}) and Cu species using Gaussian functions (6).[88] Each deconvoluted spectrum is accompanied by a lower panel depicting the fitting quality and residuals, thereby demonstrating the accuracy of the deconvolution process via the FITYK software.

$$\varepsilon_2 = \begin{cases} \dfrac{AE_0 C(E - E_g)^2}{(E^2 - E_0{}^2)^2 + C^2 E^2} \dfrac{1}{E} & \text{for } E > E_g \\ 0 & \text{for } E \leq E_g \end{cases} \tag{5}$$

where $\varepsilon_2(E)$ is the imaginary part of the dielectric function, E is the photon energy, E_g is the indirect bandgap of anatase, E_0 is the peak transition energy, C is the broadening parameter and A is the amplitude parameter.

$$f(E) = A \exp\left(-\frac{(E - E_0)^2}{2\sigma^2}\right) \tag{6}$$

where A is the amplitude, E_0 is the peak center energy and σ is the standard deviation.

For the measurements conducted during the all-solid-state photochemical study, $BaSO_4$ was not used in order to clearly display the photo-induced changes on the catalyst surface in the visible and IR regions. This also avoided any alterations in the spectra caused by interactions of the catalyst with $BaSO_4$.

Transmission Electron Microscopy (TEM) was conducted using an FEI Talos F200i field-emission gun (scanning) transmission electron microscope (Thermo Fisher Scientific Inc., Waltham, MA, USA) operated at 200 kV equipped with a windowless energy-dispersive spectroscopy microanalyzer (6T/100 Bruker, Hamburg Germany). Sample preparation involved the drop-casting of ethanolic suspensions of each catalyst onto nickel grids. Size distributions of the studied nanostructures were calculated by measuring the dimensions of an average of 80 individual nanoparticles using ImageJ software.

39872 | J. Mater. Chem. A, 2025, **13**, 39859–39876

This journal is © The Royal Society of Chemistry 2025

For the detection of copper species on the surface of TiO_2 nanoparticles, a JEOL-JEM-F200 TEM/STEM equipped with a cold field emission gun at an acceleration voltage of 200 kV, a high-angle annular dark-field (HAADF) detector used in scanning mode (STEM), and a large windowless JEOL Centurio EDX detector (100 mm², 0.97 srad, energy resolution <133 eV) was used. For sample preparation, an ethanolic dispersion of the powdered sample was prepared followed by deposition on a 400-mesh gold grid with a lacey carbon thin film (Plano GmbH). Prior to analysis, the samples were treated with a plasma cleaner (Zepto, Electronic Diener) at 20 W for 15 s at a helium (He) gas pressure of 0.03 mbar.

Inductively Coupled Plasma Optical Emission Spectrometry (ICP-OES) was employed for the accurate determination of copper content in the bulk of each sample. An Agilent 4210 Microwave Plasma Atomic Emission Spectrometer (MP-AES) at an analytical wavelength of 327.395 nm, with a calibration range of 0.5 to 10 mg l^{-1} was used. The digestion method for the (1–4) Cu-CS@TiO_2 (sr) was obtained from ref. 89 and applied with minor modifications. Briefly, 10 mg of each copper-containing sample was digested using a solution of 2.5 ml HNO_3, 2.5 ml H_2O_2 and 1 ml HF. The dispersion was heated on a hot plate at 90 °C for 3 hours and then diluted to a final volume of 50 ml with Milli-Q H_2O, in order to decrease the concentration of highly corrosive HF and HNO_3 in the final solution.

Gas-Chromatography (GC) was carried out for the identification of the products from methanol oxidation, present in the catalyst dispersion. A Chromatec Crystal 9000 GC equipped with a flame ionization detector (FID) was employed. Helium (He) was used as the carrier gas, and nitrogen (N_2) was employed as the make-up gas. The injector temperature was set to 220 °C. The oven temperature was initially held at 40 °C for 5 min, followed by a ramp of 15 °C min^{-1} to 100 °C, a subsequent ramp of 30 °C min^{-1} to 240 °C, and a final hold at 240 °C for 3 min. The FID was operated at 300 °C. Identification of the compounds was performed using external standards. For analysis, aliquots were withdrawn from the reaction mixture at specified time intervals. To remove the catalyst, each aliquot was first centrifuged and then filtered through a 0.22 μm syringe filter. A 20 μl volume of the resulting supernatant was diluted to a final volume of 1 ml with MeCN, which served as the solvent for the GC analysis.

Photoelectrochemical measurements were performed using a standard three-electrode using VersaSTAT 3 Potentiostat/Galvanostat (AMETEK, Inc., USA), controlled by VersaSTAT software for data acquisition and analysis. A Fluorine-doped Tin Oxide (FTO) glass (1 cm × 1 cm) coated with each catalyst served as the working electrode. A Pt wire and an Ag/AgCl (saturated KCl) electrode were used as the counter and reference electrode, respectively. The working electrode was prepared by dispersing 5 mg of the catalyst powder in 1 ml of a 1% v/v Nafion, ethanolic solution, followed by ultrasonication for 10 min to form the catalyst ink. The catalyst was drop-cast on the FTO substrate and dried overnight at 60 °C. A 300 W Xe lamp (100 mW cm^{-2}) was used as the light source. A 0.2 M Na_2SO_4 solution was employed as the electrolyte. Photocurrent density $vs.$ time (J–t) curves were measured using

a chronoamperometric method at a constant bias of 0.5 V $vs.$ Ag/AgCl under light illumination on and off cycles of 20 s each.

Electrochemical Impedance Spectroscopy (EIS) analysis was conducted in the frequency range of 10 kHz to 0.01 Hz with an AC amplitude of 5 mV at the open-circuit potential.

Apparent Quantum Yield (AQY%) values were obtained in order to evaluate the utilization of incident photons by the better performing photocatalyst. A 300 W Xe lamp was used as the light source, coupled with bandpass filters (Coligh Optics, 340 ± 5 nm, 390 ± 5 nm) to isolate specific wavelengths. The incident photon flux (P) for each center wavelength was measured at the reactor position using an optical power meter (Achema, 73927). The number of incident photons (N_p) was calculated using the following formula:

$$N_p = \frac{P\lambda t}{hc} \tag{7}$$

where P is the power in W measured at each wavelength, λ is the center wavelength of each bandpass filter, t is the irradiation time (s), h is Planck's constant (6.626×10^{-34} J s), and c is the speed of light (2.998×10^8 m s^{-1}).[35] The calculation then was performed using the formula:

$$AQY\ (\%) = \frac{2 \times number\ of\ evolved\ H_2\ molecules}{N_p} \tag{8}$$

3.4 Experimental procedures

3.4.1 Photocatalytic hydrogen evolution. The photocatalytic hydrogen evolution reaction (HER) was conducted using a 300 W Xe lamp solar-light simulator. The evaluation of the most active catalyst and its in-solution stability after one year was performed using the following experimental setup: a gas-tight 15 ml glass vial was filled with a 200 μg ml^{-1} nanocatalyst dispersion in Milli-Q H_2O, occupying 70% of the total volume. Methanol, at an H_2O/methanol ratio of 80 : 20, was used as the sacrificial electron donor. The nanocatalyst dispersion was degassed for 15 minutes under an Ar flow. To maintain a stable temperature and filter wavelengths below 200 nm, a water-circulating Pyrex cold filter was employed. The photocatalytic reactor was positioned 50 cm from the lamp, and the reaction was carried out at 300 rpm for 6 hours. For hydrogen quantification, 100 μl of the gaseous mixture from the reactor headspace was sampled hourly using a gas-tight syringe and analyzed with a gas chromatograph (Bruker 430-GC) equipped with a thermal conductivity detector (TCD). The oven and detector temperatures were set to 70 °C and 150 °C, respectively. A 5 Å molecular sieve column was used, with nitrogen (N_2) as the carrier gas. Data acquisition and quantification were performed using Galaxie (Varian) software. Calibration of the gas chromatograph was achieved as described before.[90]

To determine the rate-limiting component between the sacrificial donor and the catalyst, an extended-duration experiment was conducted. The quantities of catalyst and solvent mixture were reduced by 25%, while maintaining the same catalyst-to-solvent ratio. This adjustment was made to prevent

This journal is © The Royal Society of Chemistry 2025

J. Mater. Chem. A, 2025, **13**, 39859–39876 | **39873**

over-pressurization of the gas-tight vial and ensure the reproducibility of the method.

To evaluate the photocatalytic activity under softer irradiation conditions ($\lambda > 380$ nm), 10 mg of the powdered photocatalyst were dispersed by ultrasonication in a 20% MeOH solution with a total volume of 40 ml. The suspension was then transferred to a reaction chamber which was evacuated and subsequently filled with Ar to a pressure of 1.2 bar. The reaction was carried out under visible light illumination with a 300 W solar simulator (Quantum Design) using a 380 nm cutoff filter and an AM 1.5G filter, while the dispersion was continuously stirred at 300 rpm. The evolved H_2 was quantified by gas chromatography (Micro GC Fusion, Inficon) by taking a measurement every 30 minutes for a total reaction time of 3 hours.

3.4.2 All solid-state photochemical analysis. The photochemical all-solid-state analysis of the catalysts was conducted using a custom-designed experimental set-up. For sample preparation, a round steel sample holder with a 2.6 mm diameter was employed. Initially, a stainless-steel sample holder with a cavity was utilized, which was filled nearly to the top with $BaSO_4$ to create a uniform background. Subsequently, a circular quartz glass slide of equal diameter was affixed, and a uniform catalyst layer was prepared on its surface *via* drop casting. To construct the catalyst film, 30 mg of the catalyst were dispersed in 5 ml of MeOH, resulting in a homogeneous film on the quartz glass.

The experimental setup was assembled inside a fume hood as follows: the sample holder was positioned 0.5 m away from the Xe lamp, with a quartz filter placed in between to block wavelengths below 200 nm. A methanol reflux was set in a Schlenk flask while Ar gas was fed through the top of the condenser. The whole device was placed adjacent to the catalyst film. A gas-injection nozzle was used to direct the flow of Ar and methanol vapors toward the catalyst surface with a fixed rate of 3 ml of gaseous mixture per hour. The flask was evacuated after every time point to avoid over-pressurization. Since methanol is flammable, and its vapor can cause irritation to the eyes and skin, all experiments were conducted inside a fume hood. After 30 min intervals of irradiation, the sample holder was removed for absorbance UV-DRS measurements. XRD analysis was conducted on the powdered catalyst before and after the experiment.

4. Conclusions

In summary, we report an innovative synthetic approach to fabricate TiO_2-supported photocatalysts with finely controlled, multivalent Cu active sites ($Cu^0/Cu^{1+}/Cu^{2+}$) for efficient hydrogen evolution through water reduction and methanol reforming to formaldehyde. The resulting catalysts demonstrate exceptional HER activity under both full-solar and near UV-visible irradiation, remarkable stability during extended operation, and structural integrity of the active sites. Comprehensive structural and spectroscopic characterization revealed distinct Cu valence states emerging from varying Cu loadings, while elucidating the critical role of $NaBH_4$ reduction in fostering strong metal–support interactions that enhance photocatalytic performance. Systematic *operando* analysis of the optimal 3Cu-CS@TiO$_2$ (sr) catalyst in its solid form provided insight into the dynamic $Cu^{2+} \rightarrow Cu^{1+} \rightarrow Cu^0 \rightarrow Cu^{2+}$ redox cycle, where Cu^{2+} serves as the primary electron mediator, and Cu^{1+} as well as Cu^0 nanoparticles function as the dominant active sites for proton reduction to H_2. This solid-state photochemical approach establishes a new methodology for probing surface reaction mechanisms in photocatalysis, offering unique advantages for understanding charge transfer processes at metal–semiconductor interfaces under operational conditions.

Author contributions

Panagiotis Tzevelekidis: writing – original draft, investigation, formal analysis, data curation, visualization. Elias Sakellis: investigation. Nikos Boukos: investigation. Alexandros K. Bikogiannakis: investigation. Georgios Kyriakou: formal analysis. Jakob Praxmair: investigation. Gregor A. Zickler: investigation. Simone Pokrant: resources. Christiana A. Mitsopoulou: project administration, conceptualization, funding acquisition, supervision, resources, writing – review & editing. All authors discussed the results and contributed to the final draft of the paper.

Conflicts of interest

There are no conflicts to declare.

Data availability

The data supporting this article have been included as part of the supplementary information (SI). Supplementary information: XPS analysis (Fig. S1); TEM, HR-TEM and the *d*-spacing of selected TiO_2 (sr) regions (Fig. S2); TEM-BF, HAADF-STEM HR-TEM, elemental mapping and the *d*-spacing of selected 1Cu-CS@TiO$_2$ regions (Fig. S3); TEM-BF, HAADF-STEM, HR-TEM, elemental mapping and the *d*-spacing of selected 2Cu-CS@TiO$_2$ regions (Fig. S4); TEM-BF, HAADF-STEM, HR-TEM, elemental mapping and the *d*-spacing of selected 4Cu-CS@TiO$_2$ regions (Fig. S5); reflectance spectra of the synthesized photocatalysts, (b) Gaussian 1 (G1) transition attributed to surface defects, (c) Gaussian 2 (G2) attributed to multi-valent Cu species, (d) Gaussian 3 (G3) attributed to multi-valent Cu species, and (e) Gaussian 4 (G4) attributed to the d–d transition of Cu^{2+}. In all cases, electronic transitions were obtained through the deconvolution of the absorbance spectra, using FITYK software (Fig. S6); (a) transient photocurrent density (PCD) and (b) EIS plots of curves of bare and Cu loaded photocatalysts (Fig. S7); gas of the reaction solution at different time-points. Aliquots were sampled at the start (0 h), 2 h, 12 h, and at the H_2 plateau time-point (26 h) during simulated solar-light irradiation. The optimal conditions were employed: 0.2 mg ml^{-1} 3Cu-CS@TiO$_2$ (sr), 20% v/v MeOH solution. (Fig. S8); PXRD patterns of fresh and used photocatalyst 3Cu-CS@TiO$_2$ (sr) from the dispersion and solid-state based experiments (Fig. S9); Apparent Quantum Yield (AQY%) values of the 3Cu-CS@TiO$_2$ (sr) photocatalyst measured at 340 ± 5 nm and $390 \pm$

39874 | *J. Mater. Chem. A*, 2025, **13**, 39859–39876

This journal is © The Royal Society of Chemistry 2025

5 nm (Fig. S10); crystallographic data obtained after Rietveld refinement of bare TiO_2 (sr) and of the Cu loaded photocatalysts, (Table S1); elemental distribution obtained from TEM-EDS and bulk copper quantification obtained from ICP-OES (Table S2). See DOI: https://doi.org/10.1039/d5ta04071j.

Acknowledgements

References

1 N. Keller, J. Ivanez, J. Highfield and A. M. Ruppert, *Appl. Catal., B*, 2021, **296**, 120320.

2 T. Taseska, W. Yu, M. K. Wilsey, C. P. Cox, Z. Meng, S. S. Ngarnim and A. M. Müller, *Top. Catal.*, 2023, **66**(5), 338–374.

3 A. Seretis, P. Diamantopoulou, I. Thanou, P. Tzevelekidis, C. Fakas, P. Lilas and G. Papadogianakis, *Front. Chem.*, 2020, **8**, 1–22.

4 A. Zarkadoulas, E. Koutsouri, C. Kefalidi and C. A. Mitsopoulou, *Coord. Chem. Rev.*, 2015, **304–305**, 55–72.

5 D. Katakis, C. Mitsopoulou and E. Vrachnou, *J. Photochem. Photobiol., A*, 1994, **81**, 103–106.

6 Q. Hassan, A. M. Abdulateef, S. A. Hafedh, A. Al-samari, J. Abdulateef, A. Z. Sameen, H. M. Salman, A. K. Al-Jiboory, S. Wieteska and M. Jaszczur, *Int. J. Hydrogen Energy*, 2023, **48**, 17383–17408.

7 H. Ishaq, I. Dincer and C. Crawford, *Int. J. Hydrogen Energy*, 2022, **47**, 26238–26264.

8 A. Zarkadoulas, E. Koutsouri and C. A. Mitsopoulou, *Coord. Chem. Rev.*, 2012, **256**, 2424–2434.

9 A. Fujishima and K. Honda, *Nature*, 1972, **238**(5358), 37–38.

10 S. A. Ali and T. Ahmad, *Mater. Today Chem.*, 2023, **29**, 101387.

11 W. Li, F. Gao, G. Liao, W. Duan, Y. Wang, R. Cui, J. Tong and C. Wang, *Chem. Eng. J.*, 2024, **492**, 152330.

12 H. Chen, C. E. Nanayakkara and V. H. Grassian, *Chem. Rev.*, 2012, **112**, 5919–5948.

13 M. Janczarek, Ł. Klapiszewski, P. Jędrzejczak, I. Klapiszewska, A. Ślosarczyk and T. Jesionowski, *Chem. Eng. J.*, 2022, **430**, 132062.

14 P. Tzevelekidis, M. Theodosiou, A. Papadopoulou, E. Sakellis, N. Boukos, A. K. Bikogiannakis, G. Kyriakou, E. K. Efthimiadou and C. A. Mitsopoulou, *Heliyon*, 2024, **10**, e35634.

15 Q. Guo, C. Zhou, Z. Ma and X. Yang, *Adv. Mater.*, 2019, **31**, 1901997.

16 K. Nanaji, R. K. Siri Kiran Janardhana, T. N. Rao and S. Anandan, *J. Alloys Compd.*, 2019, **794**, 662–671.

17 R. Chauhan, A. Kumar and R. P. Chaudhary, *Spectrochim. Acta, Part A*, 2012, **98**, 256–264.

18 X. Chen and C. Burda, *J. Am. Chem. Soc.*, 2008, **130**, 5018–5019.

19 V. C. Anitha, A. Goswami, H. Sopha, D. Nandan, M. B. Gawande, K. Cepe, S. Ng, R. Zboril and J. M. Macak, *Appl. Mater. Today*, 2018, **10**, 86–92.

20 J. Taing, M. H. Cheng and J. C. Hemminger, *ACS Nano*, 2011, **5**, 6325–6333.

21 D. V. Ponnuvelu, B. Pullithadathil, A. K. Prasad, S. Dhara, K. Mohamed, A. K. Tyagi and B. Raj, *J. Mater. Sci.: Mater. Electron.*, 2017, **28**, 9738–9748.

22 O. Mbrouk, M. Fawzy, H. M. El-Shafey, M. Saif, M. S. A. Abdel Mottaleb and H. Hafez, *RSC Adv.*, 2023, **13**, 770–780.

23 B. Sun, W. Zhou, H. Li, L. Ren, P. Qiao, W. Li and H. Fu, *Adv. Mater.*, 2018, **30**, 1–8.

24 Y. Liu, J. Tian, L. Wei, Q. Wang, C. Wang, Z. Xing, X. Li, W. Yang and C. Yang, *Sep. Purif. Technol.*, 2021, **257**, 1–10.

25 S. Naniwa, K. Kato, A. Yamakata, A. Yamamoto and H. Yoshida, *ACS Catal.*, 2023, **13**, 15212–15218.

26 X. Liang, N. Fu, S. Yao, Z. Li and Y. Li, *J. Am. Chem. Soc.*, 2022, **144**, 18155–18174.

27 Y. Cai, J. Fu, Y. Zhou, Y. C. Chang, Q. Min, J. J. Zhu, Y. Lin and W. Zhu, *Nat. Commun.*, 2021, **12**(1), 1–9.

28 J. Gao, H. bin Yang, X. Huang, S. F. Hung, W. Cai, C. Jia, S. Miao, H. M. Chen, X. Yang, Y. Huang, T. Zhang and B. Liu, *Chem*, 2020, **6**, 658–674.

29 Z. Li, Y. Yang, C. Zhang, W. Fan, G. Li, J. Fang and L. Lu, *Chem Catal.*, 2024, **4**, 100902.

30 Y. Zhang, J. Zhao, H. Wang, B. Xiao, W. Zhang, X. Zhao, T. Lv, M. Thangamuthu, J. Zhang, Y. Guo, J. Ma, L. Lin, J. Tang, R. Huang and Q. Liu, *Nat. Commun.*, 2022, **13**, 1–10.

31 R. Cui, W. Li, W. Duan, Y. Wang, Q. Gao, Y. Huang, X. Tuo, R. Li and W. Ma, *Appl. Catal. B Environ. Energy*, 2025, **378**, 125571.

32 W. Li, W. Duan, G. Liao, F. Gao, Y. Wang, R. Cui, J. Zhao and C. Wang, *Nat. Commun.*, 2024, **15**, 1–10.

33 F. Qin and W. Chen, *Chem. Commun.*, 2021, **57**, 2710–2723.

34 J. Chávez-Caiza, M. Navlani-García, J. Fernández-Catalá, A. Bhardwaj, C. M. Lousada, L. M. Belova, A. Berenguer-Murcia and D. Cazorla-Amorós, *Catal. Today*, 2025, **453**, 115273.

35 M. Fazil, S. M. Alshehri, Y. Mao and T. Ahmad, *Langmuir*, 2024, **40**, 4063–4076.

36 B. Xiao, C. Shen, Z. Luo, D. Li, X. Kuang, D. Wang, B. Zi, R. Yan, T. Lv, T. Zhou, J. Zhang and Q. Liu, *Chem. Eng. J.*, 2023, **468**, 143650.

37 H. Zou, Y. Tong, Y. Feng, Y. Zhou, J. Xiao, L. Xia, A. Guha, B. Polesso, B. Zhang, J. Liu and K. Wang, *ACS Appl. Nano Mater.*, 2024, **7**, 11680–11689.

38 B. Xiao, C. Shen, Z. Luo, D. Li, B. Zi, T. Zhou, H. Sun, M. Chen, J. Zhang, Z. Zhu, F. Liu, H. Cui and Q. Liu, *Chem. Eng. J.*, 2024, **499**, 156331.

39 H. Zheng, B. Zi, T. Zhou, G. Qiu, Z. Luo, Q. Lu, A. R. P. Santiago, Y. Zhang, J. Zhao, J. Zhang, T. He and Q. Liu, *Nanoscale Horiz.*, 2024, **9**, 1532–1542.

This journal is © The Royal Society of Chemistry 2025

J. Mater. Chem. A, 2025, **13**, 39859–39876 | **39875**

40 B. H. Lee, S. Park, M. Kim, A. K. Sinha, S. C. Lee, E. Jung, W. J. Chang, K. S. Lee, J. H. Kim, S. P. Cho, H. Kim, K. T. Nam and T. Hyeon, *Nat. Mater.*, 2019, **18**, 620–626.

41 P. Zhou, I. A. Navid, Y. Ma, Y. Xiao, P. Wang, Z. Ye, B. Zhou, K. Sun and Z. Mi, *Nature*, 2023, **613**, 66–70.

42 C. Cheng, W. H. Fang, R. Long and O. V. Prezhdo, *JACS Au*, 2021, **1**, 550–559.

43 D. Li, Y. Zhao, Y. Miao, C. Zhou, L.-P. Zhang, L.-Z. Wu, T. Zhang, D. Li, Y. Zhao, Y. Miao, C. Zhou, L.-P. Zhang, L.-Z. Wu and T. Zhang, *Adv. Mater.*, 2022, **34**, 2207793.

44 Y. Ma, Y. Ma, T. Lv, X. Deng, X. Kuang, J. Zhang, Q. Liu and Y. Zhang, *Catal. Sci. Technol.*, 2022, **12**, 3856–3862.

45 B. H. Lee, S. Park, M. Kim, A. K. Sinha, S. C. Lee, E. Jung, W. J. Chang, K. S. Lee, J. H. Kim, S. P. Cho, H. Kim, K. T. Nam and T. Hyeon, *Nat. Mater.*, 2019, **18**, 620–626.

46 W. Fang, M. Xing and J. Zhang, *Appl. Catal., B*, 2014, **160–161**, 240–246.

47 J. M. Valero, S. Obregón and G. Colón, *ACS Catal.*, 2014, **4**, 3320–3329.

48 O. A. Reutova, E. D. Fakhrutdinova, D. A. Goncharova, A. I. Stadnichenko, O. A. Stonkus, T. S. Kharlamova, V. A. Svetlichnyi and O. V. Vodyankina, *ACS Appl. Nano Mater.*, 2024, **7**, 17062–17073.

49 B. Choudhury, M. Dey and A. Choudhury, *Int. Nano Lett.*, 2013, **3**, 2–9.

50 L. Andronic and A. Enesca, *Front. Chem.*, 2020, **8**, 565489.

51 T. S. Rajaraman, V. G. Gandhi, V. H. Nguyen and S. P. Parikh, *Appl. Nanosci.*, 2023, **13**, 3925–3944.

52 A. A. Kashale, P. K. Dwivedi, B. R. Sathe, M. V. Shelke, J. Y. Chang and A. V. Ghule, *ACS Omega*, 2018, **3**, 13676–13684.

53 M. Sahoo, A. K. Yadav, S. N. Jha, D. Bhattacharyya, T. Mathews, N. K. Sahoo, S. Dash and A. K. Tyagi, *J. Phys. Chem. C*, 2015, **119**, 17640–17647.

54 J. Navas, A. Sánchez-Coronilla, T. Aguilar, N. C. Hernández, D. M. De Los Santos, J. Sánchez-Márquez, D. Zorrilla, C. Fernández-Lorenzo, R. Alcántara and J. Martín-Calleja, *Phys. Chem. Chem. Phys.*, 2014, **16**, 3835–3845.

55 Y. Xu, S. Wu, P. Wan, J. Sun and Z. D. Hood, *RSC Adv.*, 2017, **7**, 32461–32467.

56 A. Litke, Y. Su, I. Tranca, T. Weber, E. J. M. Hensen and J. P. Hofmann, *J. Phys. Chem. C*, 2017, **121**, 7514–7524.

57 M. Heinen, Z. Jusys and R. J. Behm, *J. Phys. Chem. C*, 2010, **114**, 9850–9864.

58 S. A. Khan, S. B. Khan, L. U. Khan, A. Farooq, K. Akhtar and A. M. Asiri, *Handbook of Materials Characterization*, 2018, pp. 317–344.

59 L. M. P. Lima, D. Esteban-Gómez, R. Delgado, C. Platas-Iglesias and R. Tripier, *Inorg. Chem.*, 2012, **51**, 6916–6927.

60 X. Chen, X. Wang and D. Fang, *Fullerenes, Nanotub. Carbon Nanostruct.*, 2020, 1048–1058.

61 M. C. Biesinger, B. P. Payne, B. R. Hart, A. P. Grosvenor, N. S. McIntryre, L. W. M. Lau and R. S. C. Smart, *J. Phys.:Conf. Ser.*, 2008, **100**, 012025.

62 J. Liu, B. Liu, Y. Ren, Y. Yuan, H. Zhao, H. Yang and S. Liu, *J. Mater. Chem. A*, 2019, **7**, 14761–14775.

63 M. J. Islam, M. Granollers Mesa, A. Osatiashtiani, J. C. Manayil, M. A. Isaacs, M. J. Taylor, S. Tsatsos and G. Kyriakou, *Appl. Catal., B*, 2021, **299**, 120652.

64 M. C. Biesinger, L. W. M. Lau, A. R. Gerson and R. S. C. Smart, *Appl. Surf. Sci.*, 2010, **257**, 887–898.

65 M. C. Biesinger, *Surf. Interface Anal.*, 2017, **49**, 1325–1334.

66 H. Huang, D. Y. C. Leung and D. Ye, *J. Mater. Chem.*, 2011, **21**, 9647–9652.

67 P. Zhang, C. Liu, X. Yang, M. Chi, L. Zhang, Y. Han, W. Zhang, S. Du and S. Liu, *J. Catal.*, 2024, **430**, 115321.

68 R. Raciti, R. Bahariqushchi, C. Summonte, A. Aydinli, A. Terrasi and S. Mirabella, *J. Appl. Phys.*, 2017, **121**, 36.

69 N. S. Kovalevskiy, M. N. Lyulyukin, D. V. Kozlov and D. S. Selishchev, *Mendeleev Commun.*, 2021, **31**, 644–646.

70 M. Chen, J. Chen, C. Chen, C. Zhang and H. He, *Appl. Catal., B*, 2022, **300**, 120735.

71 M. Chen, H. Wang, X. Chen, F. Wang, X. Qin, C. Zhang and H. He, *Chem. Eng. J.*, 2020, **390**, 124481.

72 P. Zhang, C. Liu, X. Yang, M. Chi, L. Zhang, Y. Han, W. Zhang, S. Du and S. Liu, *J. Catal.*, 2024, **430**, 115321.

73 B. Xiao, C. Shen, Z. Luo, D. Li, X. Kuang, D. Wang, B. Zi, R. Yan, T. Lv, T. Zhou, J. Zhang and Q. Liu, *Chem. Eng. J.*, 2023, **468**, 143650.

74 Z. Wang, D. Brouri, S. Casale, L. Delannoy and C. Louis, *J. Catal.*, 2016, **340**, 95–106.

75 O. A. Reutova, E. D. Fakhrutdinova, D. A. Goncharova, A. I. Stadnichenko, O. A. Stonkus, T. S. Kharlamova, V. A. Svetlichnyi and O. V. Vodyankina, *ACS Appl. Nano Mater.*, 2024, **7**, 17062–17073.

76 Y. Ma, Y. Ma, T. Lv, X. Deng, X. Kuang, J. Zhang, Q. Liu and Y. Zhang, *Catal. Sci. Technol.*, 2022, **12**, 3856–3862.

77 Y. Zhang, Y. Li, H. Yu, K. Yu and H. Yu, *J. Mater. Sci. Technol.*, 2022, **106**, 139–146.

78 B. Choudhury and A. Choudhury, *Phys. E*, 2014, **56**, 364–371.

79 T. Čižmar, I. Panžić, I. Capan and A. Gajović, *Appl. Surf. Sci.*, 2021, **569**, 151026.

80 D. Li, Y. Zhao, Y. Miao, C. Zhou, L. P. Zhang, L. Z. Wu and T. Zhang, *Adv. Mater.*, 2022, **34**, 2207793.

81 G. Y. Yao, Z. Y. Zhao, Q. L. Liu, X. D. Dong and Q. M. Zhao, *Sol. Energy Mater. Sol. Cells*, 2020, **208**, 110385.

82 A. S. Stefanarou and C. V. Chrysikopoulos, *Water*, 2021, **13**, 1420.

83 X. Yan, L. Zhao, Y. Huang and J. Zhang, *Sep. Purif. Technol.*, 2025, **354**, 128709.

84 B. H. Lee, S. Park, M. Kim, A. K. Sinha, S. C. Lee, E. Jung, W. J. Chang, K. S. Lee, J. H. Kim, S. P. Cho, H. Kim, K. T. Nam and T. Hyeon, *Nat. Mater.*, 2019, **18**(6), 620–626.

85 S. Xu, X. Huang and H. Lu, *Fuel Process. Technol.*, 2024, **255**, 108057.

86 H. Wang, E. Harkou, A. Constantinou, S. M. Al-Salemc, G. Manos and J. Tang, *Chem. Soc. Rev.*, 2025, **54**, 2188–2207.

87 H. Chen and W. Z. Shen, *Eur. Phys. J. B*, 2005, **43**(4), 503–507.

88 L. Antonov and D. Nedeltcheva, *Chem. Soc. Rev.*, 2000, **29**, 217–227.

89 I. de la Calle, M. Menta, M. Klein and F. Séby, *Talanta*, 2017, **171**, 291–306.

90 F. Kamatsos, M. Drosou and C. A. Mitsopoulou, *Int. J. Hydrogen Energy*, 2021, **46**, 19705–19716.

39876 | *J. Mater. Chem. A*, 2025, **13**, 39859–39876

This journal is © The Royal Society of Chemistry 2025